iScience

Article

SLP2 and MIC13 synergistically coordinate MICOS assembly and crista junction formation

Graphical abstract

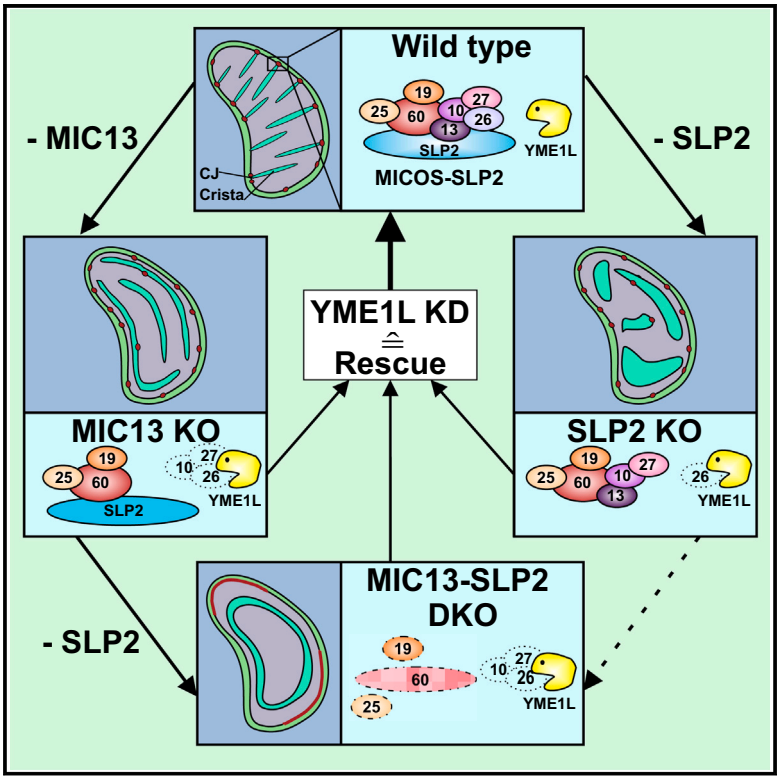

Highlights

- MIC13, mutated in mitochondrial hepato-encephalopathy, stabilizes MIC10-subcomplex
- SLP2 interacts with MIC13 and form large interaction hub with MICOS subunits
- SLP2 is essential for maintaining cristae morphology and MIC26 stability
- SLP2 and MIC13 synergistically regulate MICOS-MIB assembly and cristae formation

Authors

Ritam Naha, Rebecca Strohm, Yulia Schaumkessel, ..., Andreas S. Reichert, Arun Kumar Kondadi, Ruchika Anand

Correspondence

anand@hhu.de

In brief

Molecular biology; Cell biology

Naha et al., 2024, iScience 27, 111467
December 20, 2024
https://doi.org/10.1016/j.isci.2024.111467

CellPress

iScience

CellPress
OPEN ACCESS

Article

SLP2 and MIC13 synergistically coordinate MICOS assembly and crista junction formation

Ritam Naha,[1] Rebecca Strohm,[1] Yulia Schaumkessel,[1] Jennifer Urbach,[1] Ilka Wittig,[2,3] Andreas S. Reichert,[1] Arun Kumar Kondadi,[1] and Ruchika Anand[1,4,*]

[1]Institute of Biochemistry and Molecular Biology I, Medical Faculty and University Hospital Düsseldorf, Heinrich Heine University Düsseldorf, 40225 Duesseldorf, Germany

[2]Functional Proteomics, Institute for Cardiovascular Physiology, Faculty of Medicine, Goethe-University, 60590 Frankfurt am Main, Germany

[3]German Center of Cardiovascular Research (DZHK), Partner Site RheinMain, 60590 Frankfurt am Main, Germany

[4]Lead contact

*Correspondence: anand@hhu.de

https://doi.org/10.1016/j.isci.2024.111467

SUMMARY

The MICOS complex, essential for cristae organization, comprises MIC10 and MIC60 subcomplexes, with MIC13 as a crucial subunit. *MIC13* mutations cause severe mitochondrial hepato-encephalopathy, cristae defects, and MIC10-subcomplex loss. We demonstrate that depletion of the mitochondrial protease YME1L in *MIC13* KO stabilizes MIC10-subcomplex, restoring MIC60-MIC10 interaction and crista junction (CJ) defects, indicating MIC13 is crucial for MIC10-subcomplex stabilization rather than MIC60-MIC10 bridging. We identified stomatin-like protein 2 (SLP2) as a key MIC13 interaction partner, essential for cristae morphology and CJ formation. SLP2 serves as an interaction hub for MICOS subunits and stabilizes MIC26 by protecting it from YME1L-mediated degradation. Deleting both *SLP2* and *MIC13* impairs MIC60-subcomplex assembly and its nanoscale organization. Restoring the MIC10-subcomplex in *MIC13-SLP2* double KO cells through YME1L depletion reinstates MIC60-subcomplex assembly and cristae morphology. Overall, we propose SLP2 and the MIC10-subcomplex act as a proteolytically controlled 'seeder' complex, facilitating MICOS-MIB complex assembly and maintaining mitochondrial integrity.

INTRODUCTION

Mitochondria, known for their multifaceted roles beyond energy conversion, perform vital functions such as calcium signaling, lipid metabolism, reactive oxygen species (ROS) production, amino acid metabolism, iron-sulfur cluster synthesis, and apoptosis regulation.[1] The inner membrane (IM) of mitochondria is highly adaptable, shaping itself according to the bioenergetic demands of the cell. Cristae are infoldings of the IM that provide the characteristic wrinkled shape of IM and offer large surface area for housing electron transport chain (ETC) complexes. In the 1990s, electron tomography techniques illustrated the intricate three-dimensional (3D) arrangement of the IM and proposed the crista junction (CJ) model,[2] designating CJs as small, highly curved openings at the neck of individual cristae with a high inward-directed curvature. Due to their minute diameter, CJs were proposed to function as diffusion barriers,[2,3] subdividing mitochondria into distinct subcompartments and thus modulating several mitochondrial functions, including lipid transfer and metabolite exchange. Markedly, during apoptosis, CJ remodeling facilitates cytochrome *c* release, initiating the apoptotic cascade.[4] Yet, how these intricate structures of cristae and CJs with steep membrane curvatures are formed and remodeled remained elusive for decades. Several recent findings shed light on this significant yet technically challenging question. The 'mitochondrial contact site and cristae organizing system' (MICOS) complex has emerged as a crucial orchestrator in cristae and CJ formation.[5–8] Live-cell super-resolution (SR) nanoscopy showed that cristae and CJ are highly dynamic and undergo cycles of fusion and fission at a timescale of seconds in a MICOS-dependent manner.[9]

The mammalian MICOS complex comprises seven subunits namely MIC10, MIC13, MIC19, MIC25, MIC26, MIC27, and MIC60, that form two distinct subcomplexes, MIC60-subcomplex (MIC60-MIC19-MIC25) and MIC10-subcomplex (MIC10-MIC13-MIC26-MIC27), each contributing uniquely to mitochondrial integrity. Deletion of individual MICOS subunits results in varying degrees of aberrant cristae morphology, often leading to the accumulation of cristae stacks or, in some cases, concentric rings.[8,9] While MIC60 and MIC10 are core subunits harboring membrane remodeling abilities,[10–14] MIC13 acts as a critical bridge, modulating interactions within the complex and impacting cristae morphology.[15–18] MIC19 and MIC25, belonging to coiled-coil helix coiled-coil helix (CHCH) family proteins, assist MIC60 in CJ and contact site formation,[19,20] whereas MIC26 and MIC27, belonging to the apolipoprotein family, are essential for maintaining cristae structure and integrity of ETC complexes.[21] The interaction of the MICOS subunits with the outer membrane (OM) localized proteins SAMM50, metaxin1 (MTX1), metaxin2 (MTX2) and DNAJC11 leads to formation of the

'mitochondrial intermembrane space bridging' (MIB) complex.[22–24] MIB facilitates the contacts between IM and OM, essential for overall mitochondrial function and structural integrity.

MIC13, a key subunit of the MICOS complex, lacks comprehensive characterization and shows no resemblance to other protein families or domains.[17] Depletion of MIC13 affects cristae morphology and causes concomitant total loss of MIC10, MIC26 and partial loss of MIC27, making it difficult to delineate the specific roles of these proteins.[15,16] Previously, we have identified two critical motifs within the MIC13, namely the 'GXXXG' and the 'WN' motif, essential for its stability and functionality.[17] Nevertheless, it is an important component of the MICOS complex and mutations in *MIC13* are associated with a severe form of mitochondrial hepato-encephalopathy in pediatric patients, leading to the untimely demise, often within few months to five years.[25–27] The patients show multi-system failure affecting the brain, liver, kidney and heart.[25–28] Neurological defects include cerebellar and optic atrophy, acquired microcephaly and hypotonia, while liver complication frequently leads to acute liver failure. Increased plasma levels of lactic acid, methionine, tyrosine and Krebs cycle intermediates as well as increased excretion of 3-methylglutaconic acid were reported. In all the documented cases, MIC13 levels were not detectable, indicating the complete loss of MIC13 in these pathologies.

While mutations in MICOS subunits, including MIC60, MIC26, and notably MIC13, have been associated with severe mitochondrial diseases,[25–27,29–32] a comprehensive understanding of the underlying pathobiology, particularly for non-ETC genes, remains limited. These mitochondrial diseases, a subset of rare metabolic errors affecting 1.6 in 5000 individuals, lack effective treatments (Stenton & Prokisch, 2020). In this study, we aim to unravel the molecular role of MIC13 in cristae and CJ formation within the MICOS complex, which offer fresh insights into severe mitochondrial disorders for potential therapeutic methods.

Depletion of MIC13 results in the loss of MIC10-subcomplex making it difficult to discern whether the defects are due to loss of MIC13 or MIC10. To address this, we stabilized the MIC10-subcomplex in *MIC13* KO by depleting YME1L. Remarkably, restoring MIC10-subcomplex re-established the interaction between the MIC60 and MIC10-subcomplex and re-formed CJs. This highlights the specific role of MIC13 in stabilizing the MIC10-subcomplex against proteolytic degradation by YME1L, rather than merely acting as a bridge between the two subcomplexes. We further aimed to decipher the role of MIC13 by mapping its interactome. Employing mass spectrometry (MS) coupled with co-immunoprecipitation (co-IP) of MIC13, we identified Stomatin-like protein 2 (SLP2) as a highly enriched protein within the MIC13 interactome. Not previously linked to MICOS regulation, SLP2 forms a stable interaction hub with all the MICOS subunits and its depletion severely influences the cristae morphology. SLP2 stabilizes MIC26 by preventing YME1L-mediated degradation. It plays a distinct and essential role in modulating the assembly kinetics of MIC60. The simultaneous depletion of MIC13 and SLP2 accentuates deficiencies in MIC60-subcomplex and MIB assembly, emphasizing their collaborative roles in controlling assembly kinetics and formation of MIC60 punctae. MIC13 is specifically required to stabilize the MIC10-subcomplex, which in turn promotes MIC60-subcomplex assembly, highlighting the interdependence between assembly of MICOS subcomplexes. SLP2 plays a unique role in assisting MIC10-subcomplex in facilitating the MIC60-subcomplex assembly, therefore we termed SLP2-MIC10-subcomplex as 'seeder' complex that promotes the efficient incorporation or 'seeding' of MIC60-subcomplex into the MICOS-MIB complex. This process ensures mitochondrial integrity and the establishment of CJs and contacts between IM and OM.

RESULTS

MIC13 primarily stabilizes MIC10-subcomplex to promote crista junction formation

MIC13 has been suggested as a bridge connecting the MIC60-subcomplex and MIC10-subcomplex.[16] However, it has been difficult to identify the precise molecular role of MIC13 because *MIC13* KO was always associated with loss of the MIC10-subcomplex making it hard to differentiate whether the effects were arising due to MIC10 or MIC13 loss. In order to clarify the specific role of MIC13 for MICOS assembly, we aimed to distinguish the function of MIC13 from MIC10. Efforts to generate stable cell line expressing MIC10 in the absence of MIC13 proved challenging, perhaps because of the tendency of overexpressed MIC10 to undergo rapid degradation in the absence of MIC13. To counter this, we aimed to restore MIC10 levels by preventing its degradation in *MIC13* KO. We hypothesized that perhaps YME1L-mediated degradation might be responsible for MIC10 degradation in *MIC13* KO, given that MICOS is located in the IM facing the intermembrane space where YME1L exerts its action. To solve this, we generated stable cell lines expressing YME1L-targeted shRNA in WT and *MIC13* KO cell lines. (Figure 1A). YME1L knockdown resulted in elevated levels of MIC10 (along with MIC26 and MIC27) in WT and *MIC13* KO, showing that MIC10 (along with MIC26 and MIC27) are YME1L substrates (Figures 1A and 1B). Moreover, the restoration of MIC10 levels through YME1L downregulation in *MIC13* KO cells provided us a unique opportunity to determine the specific roles of MIC13 that are independent of MIC10. Using this approach, we checked whether the restored MIC10 could interact with MIC60. Conducting co-IP using MIC60 antibody, we analyzed the interaction of MIC60 with the replenished MIC10 in *MIC13* KO. Surprisingly, despite the absence of MIC13, when YME1L-mediated MIC10 degradation was prevented, MIC60 exhibited interactions with MIC10, MIC26 and MIC27 (Figures 1C and S1A). This finding challenges our previous understanding of MICOS assembly, suggesting that MIC13 might not be essential to bridge the two subcomplexes for MICOS assembly.[16] Instead, it appears to play a crucial role in stabilizing the MIC10-subcomplex and protect it from YME1L-dependent proteolysis. The re-established interaction of MIC60 and replenished MIC10 in the absence of MIC13 prompted us to further investigate a specific role of MIC13 in MICOS assembly.

While MIC10 levels were restored upon depletion of YME1L, a noteworthy observation emerged regarding the MIC27 band pattern specific to *MIC13* KO (Figure 1A). The MIC27 exhibited an additional, slightly lower molecular weight variant in *MIC13* KO. The identity of this MIC27 variant is yet unknown but

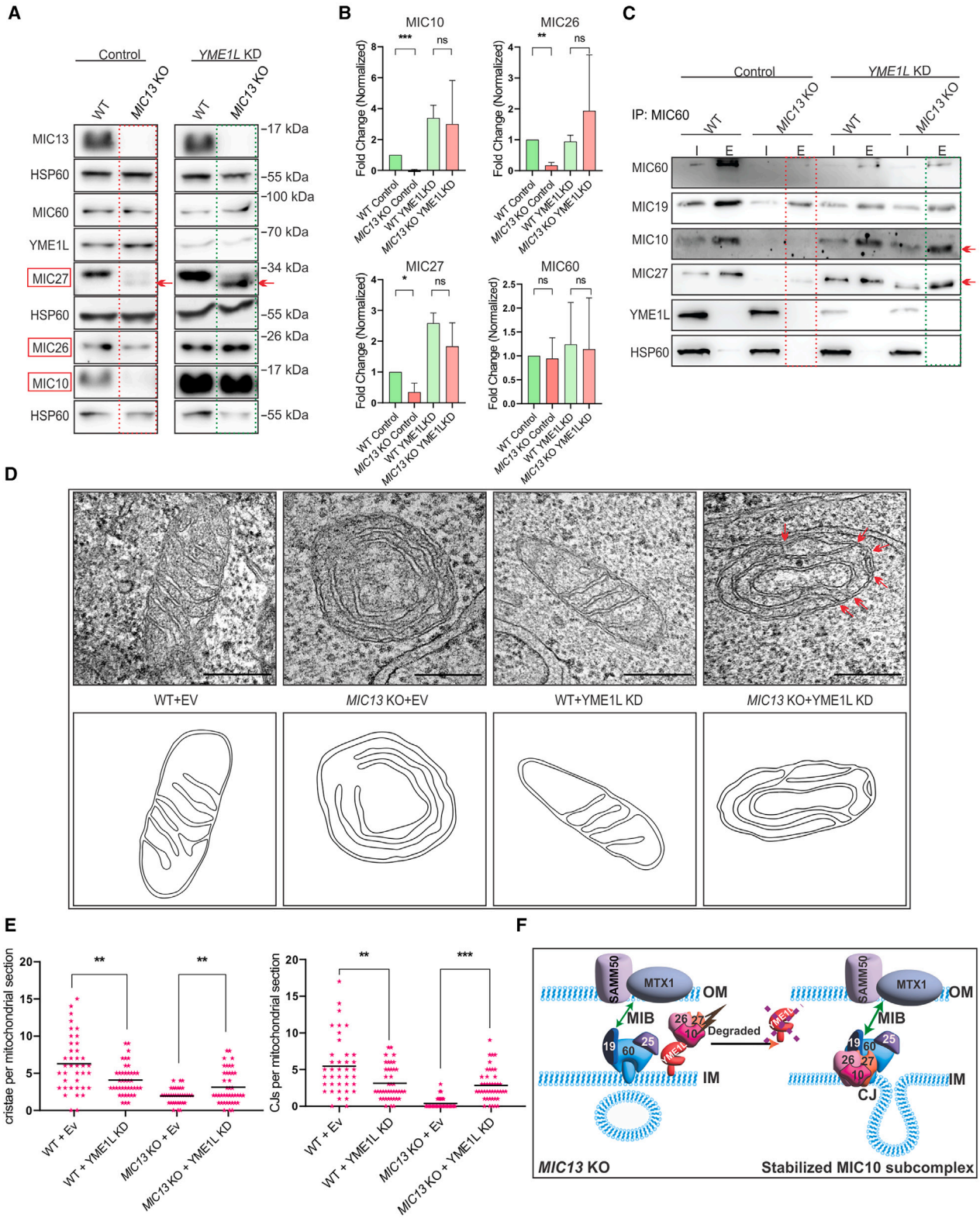

Figure 1. MIC13 primarily stabilizes MIC10-subcomplex to promote CJ formation

(A) Western blot analysis of WT and *MIC13* KO stably expressing pGIPZ-Control shRNA or pGIPZ-YME1L shRNA (knockdown represented as YME1L KD) to assess steady state levels of MICOS proteins. *MIC13* KO leads to loss of MIC10, MIC26 and MIC27, which are restored upon YME1L KD, indicating their

(legend continued on next page)

presence of this variant was solely dependent on the absence of MIC13, as it did not revert even when MIC10 (and MIC27) levels were restored. This observation highlights that MIC13 plays a unique role in managing the structural status of MIC27 independent of its influence on MIC10 levels. Overall, our findings allow us to delineate the function of MIC13 from MIC10, disproving the previous notion of MIC13 solely acting as a bridge. Instead, we reveal that MIC13 is crucial for providing stability to the entire MIC10-subcomplex by safeguarding it from the proteolytic activity of YME1L. Furthermore, our study sheds light on additional functions of MIC13, such as its role in regulating MIC27.

Next, we analyzed the effect of stabilized MIC10-subcomplex in *MIC13* KO on cristae morphology. Typically, MIC13 loss is associated with significant cristae defects and loss of CJs, resulting in stacked or concentric-ring cristae. Remarkably, restoring MIC10-subcomplex in *MIC13* KO through YME1L depletion had a moderate beneficial effect on mitochondrial ultrastructure, significantly restoring CJs (Figure 1D). The number of cristae and CJs were quantified in a double-blind manner to prevent any potential bias by the analysis (Figure 1E). The cristae in this scenario appeared to unfurl from the concentric ring-like structures and reattach to IM to form nascent CJs. This indicates that stabilized MIC10 can promote the formation of nascent CJs in *MIC13* KO (Figures 1D and 1E), highlighting the significant contribution of MIC10 in the cristae phenotype observed in *MIC13* KO (Figure 1F). This finding clarifies that primary cristae defects observed in *MIC13* KO arise from the loss of MIC10 rather than MIC13 itself. This is particularly relevant to MIC13-associated mitochondrial hepato-encephalopathy, as patient cells also exhibit concentric or stacked cristae structure (Guarani et al., 2016). The new insights in MIC13 roles, whether dependent or independent of MIC10, holds significant potential for advancing our understanding of the pathobiology underlying mitochondrial hepato-encephalopathy associated with *MIC13* mutations.

Determining the MIC13 interactome

To further unravel the elusive role of MIC13, we set out to determine the MIC13 interactome. Our methodology involved isolating mitochondria from HEK293 cells, followed by co-IP using agarose beads conjugated with MIC13 antibody. We then analyzed the eluate fraction via mass spectrometry (MS) to identify the proteins specifically and significantly enriched in wild type (WT) cells compared to *MIC13* knockout (KO) cells. The analysis revealed numerous proteins constituting the interactome of MIC13 in mammalian cells (Figure 2A; Table S1). Among these proteins were members of MICOS and MIB complex or their known interactors, emphasising the specificity of the experiment and highlighting the central role of MIC13 in MICOS-MIB regulation. Especially, our results also revealed SLP2 as a previously unknown interaction partner, exhibiting the most significant enrichment upon statistical analysis (Figure 2A). SLP2 belongs to the SPFH (stomatin, prohibitin, flotillin, HflC/K) superfamily of scaffolding proteins that can form microdomains in the membrane by local lipid-protein interactions. It can bind cardiolipin as well[33] and has been implicated in various mitochondrial functions including biogenesis, proteolysis and stress-induced mitochondrial hyperfusion (SIMH) regulation.[34] SLP2 interacts with mitochondrial proteases like PARL and YME1L, forming a large hub of proteases within the IM known as the SPY complex.[35] A direct contribution of SLP2 to MIC13/MICOS regulation and cristae morphology remains unexplored, prompting our focused investigation into this intriguing possibility.

SLP2 forms a stable interaction hub with all MICOS subunits

In order to confirm the direct interaction between MIC13 and SLP2 demonstrated by MS coupled co-IP experiment (Figure 2A), we performed western blot (WB) analysis utilizing the elution fraction obtained from MIC13-FLAG co-IP. Upon probing with an SLP2 antibody, we observed considerable increase in the intensity of the SLP2 band in *MIC13* KO cells expressing MIC13-FLAG compared to *MIC13* KO expressing an empty vector (EV), confirming the interaction of MIC13 and SLP2 (Figure 2B). The minor yet significant fraction of SLP2 physically interacted with MIC13. The specificity of this co-IP was validated by the absence of matrix protein HSP60 and ETC complex IV protein Mt-CO2 in the elution fraction (Figure 2B). We further substantiated the MIC13-SLP2 interaction by using SLP2 as bait in a co-IP experiment. For this, we generated *SLP2* KO cells using CRISPR-Cas9 system and stably expressed SLP2 with an MYC tag at its C-terminus. Co-IP was performed using MYC-trap agarose and the elution fraction was probed for antibodies

dependency on YME1L-mediated proteolysis. HSP60 serves as a loading control. The red arrow highlights the lower band of MIC27 that appears specifically in the *MIC13* KO. Although YME1L knockdown in *MIC13* KO cells restores the steady-state levels of MIC27, the persistence of the lower band suggest that this alteration is specifically linked to absence of MIC13.

(B) Western blot quantification shows relative protein levels, with values normalized to those of the WT. Data is represented as the mean ± standard error of mean ($n = 3$). Statistical analysis was performed using Student's *t* test or one sample *t*-test. **p*-value ≤0.05, ***p*-value ≤0.01, ****p*-value ≤0.001, ns = non-significant, *p*-value >0.05.

(C) The interaction between MIC60 and MIC10 was validated by co-IP using MIC60 antibody conjugated Protein A Sepharose beads in isolated mitochondria from WT and *MIC13* KO cells stably expressing pGIPZ YME1L shRNA or empty vector (EV) pGIPZ as background control. I: input lanes represent loading of 10% of total lysates, E: eluate represent proteins eluted from beads. MIC10 and MIC27, which are restored upon YME1L depletion, could still interact with MIC60 even in the absence of MIC13 (indicated by red arrow).

(D) Mitochondrial cristae morphology accessed using TEM from WT and *MIC13* KO stably expressing pGIPZ-Control shRNA or pGIPZ-YME1L shRNA. The skeletonization of the TEM image is shown below each corresponding image. Scale bar represents 0.5 μm. YME1L depletion showed beneficial consequences on cristae morphology with presence of nascent CJs (red arrows). This indicates that loss of CJs in *MIC13* KO is attributed to MIC10 loss.

(E) Cristae number and CJs per mitochondrial section quantified from TEM images. Statistical analysis was performed using Student's *t* test. ***p*-value ≤0.01, ****p*-value ≤0.001.

(F) Scheme depicting the role of MIC13 in protecting the MIC10-subcomplex from YME1L-mediated proteolysis. In absence of MIC13, the stabilized MIC10-subcomplex could still facilitate the formation of crista junctions and maintain the interaction between MIC60-subcomplex and remaining MIC10-subcomplex.

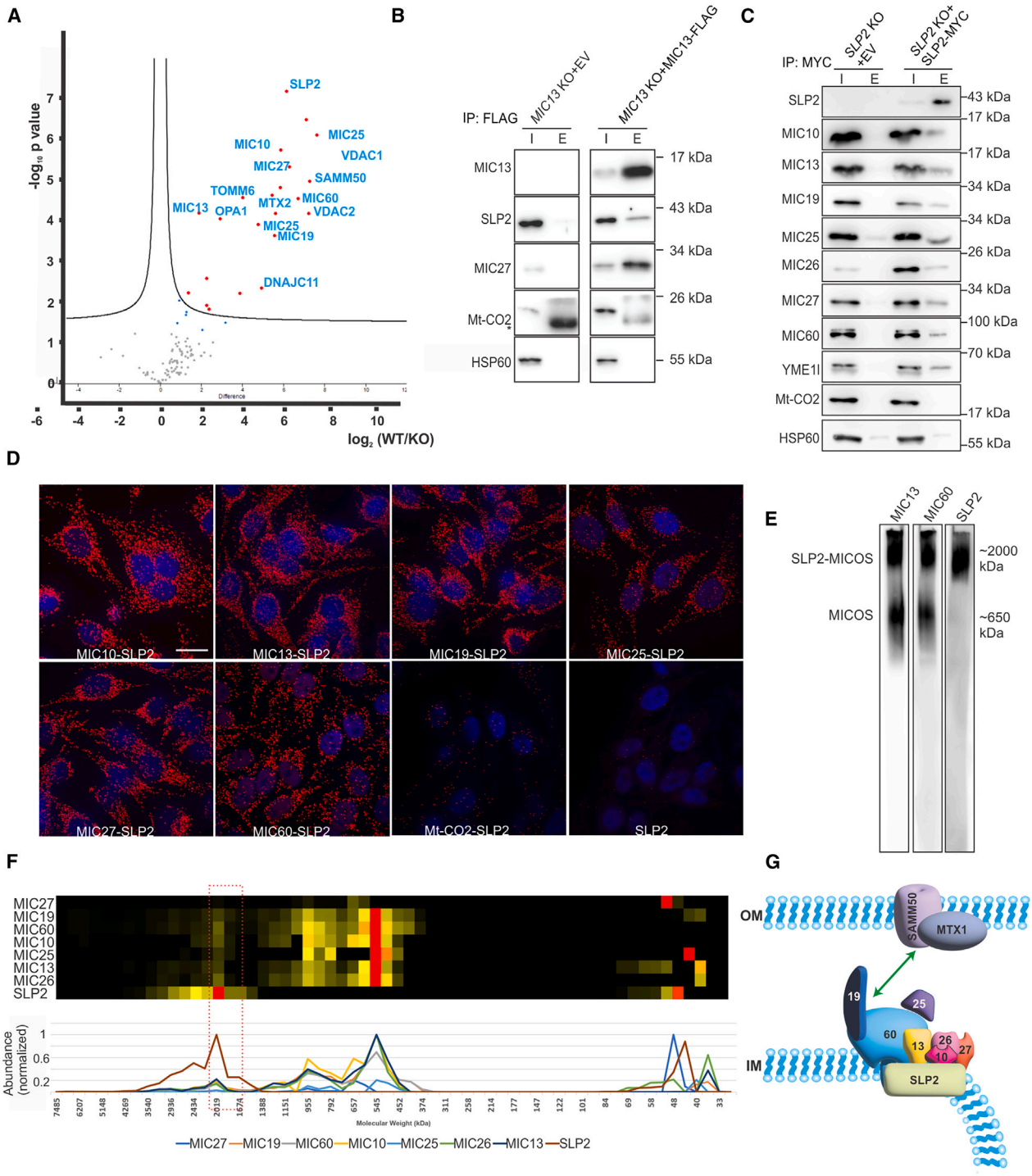

Figure 2. SLP2 is identified as an interacting partner of MIC13

(A) Interactome of MIC13 with co-IP (co-immunoprecipitation) coupled mass spectrometry revealed SLP2 as an interactor of MIC13.

(B) The interaction between SLP2 and MIC13 was confirmed by co-IP using FLAG antibody in isolated mitochondria from *MIC13* KO cells stably expressing MIC13-FLAG or empty vector (EV) pMSCVpuro as background control. I: input lanes represent loading of 10% of total lysates, E: eluate represent proteins eluted from anti-Flag M2 beads, * non-specific IgG bands.

(C) Co-IP was used to detect the SLP2-MICOS interaction using isolated mitochondria from *SLP2* KO stably expressing pMSCVpuro EV (background control) or SLP2-MYC. Co-IP was performed using MYC-Trap agarose beads. I: Input fraction (10% of total lysate), E: Eluate fraction. YME1L was used as a positive interactor of SLP2 whereas Mt-CO2 and HSP60 served as non-interactors. All the MICOS subunits were detected in the elution fraction from SLP2-MYC co-IP.

(legend continued on next page)

against SLP2, YME1L (known SLP2 interactor), and all MICOS subunits, along with HSP60 and Mt-CO2 serving as negative controls. The presence of SLP2-MYC and YME1L and the absence of HSP60 and Mt-CO2 in the elution fraction showed the specificity of the co-IP experiment (Figure 2C). All MICOS subunits, and not only MIC13, were present in the elution fraction, showing that SLP2 potentially interacts directly or indirectly with all the MICOS subunits (Figure 2C). To visually and definitively evaluate the proximity between SLP2 and individual MICOS subunits, we employed the proximity ligation assay (PLA). Using antibodies specific to SLP2 and individual MICOS subunits, we observed numerous punctae in each cell, indicating proximity between SLP2 and individual MICOS subunits, unlike in the negative controls of Mt-CO2 & SLP2 or only SLP2 antibody (Figure 2D). Overall, several lines of evidence firmly establish the specific and reciprocal interaction of SLP2 with the MICOS complex.

Considering the inherent limitations of co-IP experiments, we cannot specify whether SLP2 interacts individually with each MICOS subunit or whether there is a hierarchy in the interaction of MICOS subunits with SLP2. To determine whether the interaction between SLP2 and MICOS subunits relies on any particular MICOS subunit, we conducted co-IP experiments in cells depleted for individual MICOS subunits (Figures S1B and S1C). We generated KO cells lacking individual MICOS subunits (MIC10, MIC26, MIC27, MIC19, MIC25 and MIC60) in HEK293 cell lines and stably expressed SLP2-MYC in these cell lines. As expected, the *MIC10* KO and *MIC13* KO cells showed loss (or decrease) of all subunits of the MIC10-subcomplex (MIC10/13/26/27) while KO of either *MIC26* or *MIC27* showed no pronounced alterations in other MICOS subunits (Figure S1B). Concerning the MIC60-subcomplex, *MIC60* KO cells demonstrated a drastic decrease in steady state levels of all other MICOS subunits, whereas *MIC19* KO cells showed a complete loss of MIC10 and reduced MIC60 and MIC13 levels (Figure S1C). *MIC25* KO cells showed minimal effect on the levels of other MICOS subunits (Figure S1C). Despite the loss of MIC10-subcomplex in *MIC10* KO and *MIC13* KO cells, SLP2 sustained interactions with YME1L, MIC19, MIC25 and MIC60 (Figure S1B). Similarly, despite individual deletions of *MIC26*, *MIC27* and *MIC25*, SLP2 maintained its interaction with the remaining MICOS subunits (Figures S1B and S1C). Particularly striking was the observation in *MIC60* KO cells with substantially reduced levels of all MICOS subunits in the input fraction, SLP2 showed interactions with residual MIC13, MIC26, MIC27, and MIC19 (Figure S1C). These findings collectively suggest that SLP2 retains stable interaction with any remaining MICOS subunits despite the absence of specific individual subunits. These observations highlight the role of SLP2 as a scaffold, facilitating the formation of an interaction hub with all MICOS subunits in the IM.

Our data pointed to the formation of a large SLP2-MICOS interaction hub and therefore we employed blue native gel electrophoresis (BN-PAGE) to analyze the high-molecular weight native complexes of both SLP2 and MICOS. MICOS subunits are typically organized into two distinct complexes: a large MICOS complex (~2000 kDa) known to include MIB subunits and a lower molecular weight MICOS complex (~700 kDa).[15] Our analysis revealed that SLP2 forms a high molecular weight complex running alongside the larger MICOS complex at approximately 2000 kDa (Figure 2E). This finding aligns with the complexome profiling data derived from HEK293 cells,[15] which demonstrate the co-clustering of SLP2 and MICOS subunits within the 2000 kDa range (Figure 2F). We also observed that SLP2 remains in the high molecular weight complex even upon the deletion of *MIC60*, and similar results were seen in the complexome data from *MIC13* KO cells (Figures S2A and S2B). Overall, these diverse lines of experimentation collectively support and firmly establish the interaction between SLP2 and MICOS, elucidating their functional interplay within mitochondrial architecture (Figure 2G).

SLP2 depletion impairs cristae and crista junction formation

Subsequently, we sought to determine the significance of the SLP2-MICOS interaction by investigating whether loss of SLP2 affects the stability of MICOS subunits and the MICOS complex as a whole or cristae structure. Through WB analysis, we evaluated the levels of MICOS subunits in *SLP2* KO cells and observed a substantial reduction specifically in the steady state levels of MIC26, consistently supported by the quantitative analysis of the western blot (Figures 3A and 3B). Notably, MIC27 levels were slightly elevated, which could be attributed to the known antagonistic relationship between MIC26 and MIC27, where the loss of one typically leads to an increase in the other or vice versa.[21,36,37] The MICOS assembly using a BN-PAGE showed that MIC26 was sparsely present in the MICOS complex as expected from the steady state levels, however the incorporation of most other MICOS subunits into the MICOS complex appeared comparable to WT (Figures S3 and 3A). We analyzed whether the loss of MIC26 in *SLP2* KO cells results from proteolysis via YME1L. To test this, we employed short hairpin RNA (shRNA) to deplete YME1L in *SLP2* KO cells and indeed observed a significant rescue of the levels of MIC26 in *SLP2* KO cells (Figure 3C), indicating a specific role of SLP2 in safeguarding MIC26 from YME1L-mediated degradation.

Next, we conducted transmission electron microscopy (TEM) imaging on *SLP2* KO cells. Remarkably, the *SLP2* KO cells showed apparently swollen cristae and a substantial reduction in the number of cristae and CJs compared to WT cells (Figures 3D and 3E). Number of cristae and CJs were quantified in a double-blind fashion to eliminate any potential biases in the

(D) Proximity ligation assay (PLA) in HeLa cells with antibodies against MICOS subunits and SLP2. PLA signals are shown as red spots indicating respective protein interactions. SLP2 alone and Mt-CO2 & SLP2 antibodies were probed as negative controls. Scale bar 20 μm.
(E) BN-PAGE with isolated mitochondria from WT cells revealed a co-migration pattern of SLP2 with higher molecular weight MICOS complex.
(F) A heatmap and graph represent the normalized occurrence of SLP2 and MICOS subunits in complexome profiling data obtained from HEK293 cells studied previously.[15] SLP2 co-clustered with high molecular weight MICOS complex at around 2000 kDa.
(G) Scaffolding model depicting interaction of SLP2 with MICOS subunits shows that SLP2 provides a scaffold for interaction of MICOS subunits.

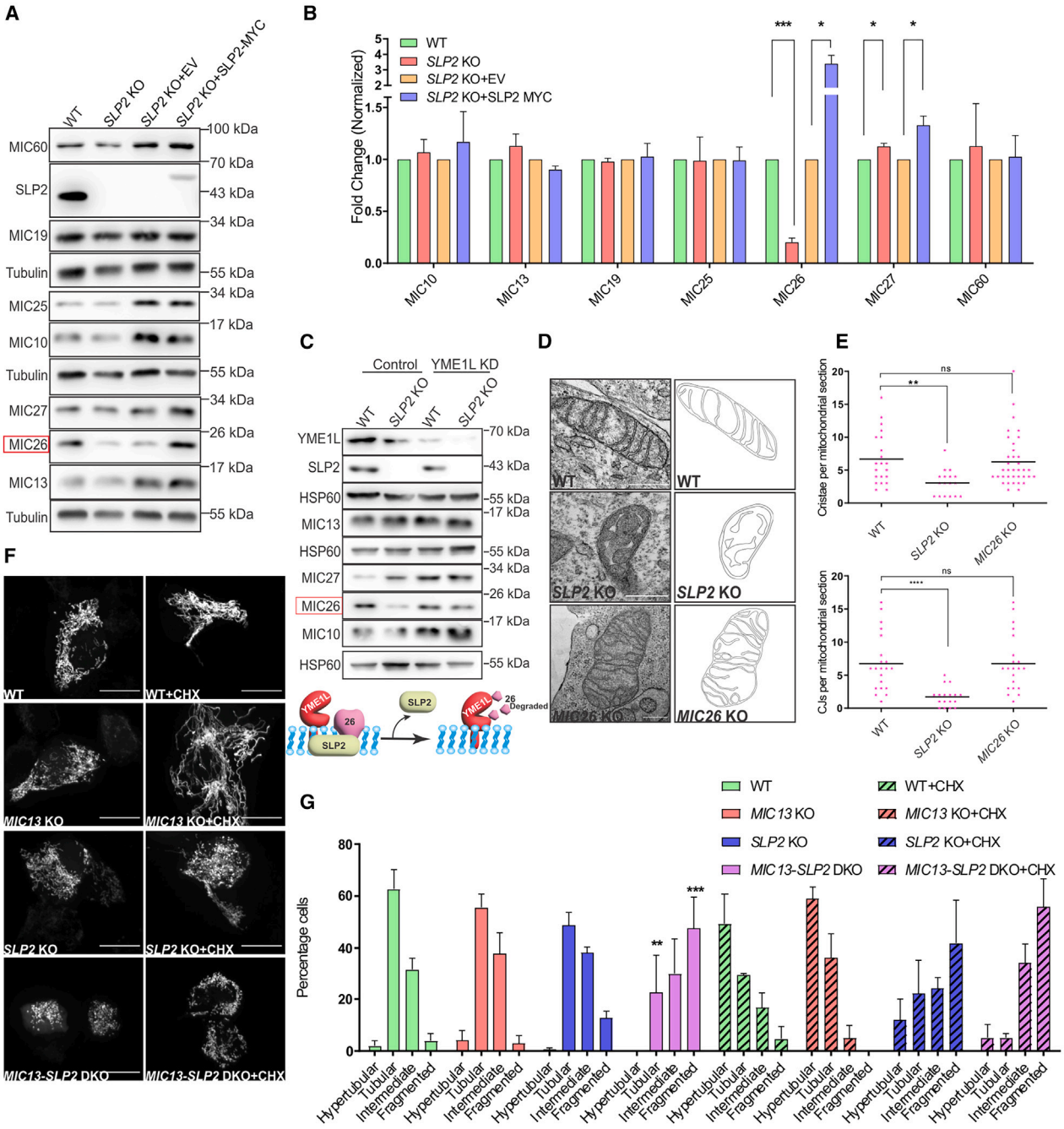

Figure 3. Loss of SLP2 leads to aberrant cristae structure and reduced MIC26 levels

(A) Steady state levels of MICOS proteins with western blot analysis from WT, *SLP2* KO and *SLP2* KO cells stably expressing pMSCVpuro EV or SLP2-MYC. Tubulin serves as a loading control for western blots.

(B) Western blot quantification depicting relative protein levels. *SLP2* KO was normalized to WT and *SLP2* KO + SLP2 MYC was normalized to *SLP2* KO + EV samples. Data is represented as mean ± standard error of mean ($n = 3$). Statistical analysis was performed using Student's *t* test. *p-value $\leq$0.05, ***p-value $\leq$ 0.001. MIC26 levels were reduced in *SLP2* KO. Notably, MIC27 levels showed a slight increase in *SLP2* KO.

(C) Western blot analysis of steady state levels of MICOS proteins from WT and *SLP2* KO cells stably expressing pGIPZ-control shRNA or YME1L shRNA. The results are depicted by a model illustrating the role of SLP2 in stabilizing MIC26 through the regulation of YME1L-mediated proteolysis. HSP60 acts as an internal protein loading control.

(D) TEM images from WT, *SLP2* KO and *MIC26* KO cells. *SLP2* KO shows loss of cristae and CJs with accumulation of swollen cristae, while *MIC26* KO shows slight cristae branching. Scale bar represents 500 nm. The skeletonization of the TEM image is depicted on right side.

(legend continued on next page)

data (Figure 3E). Cristae appeared as isolated stacks within the mitochondria, devoid of CJs. To the best of our knowledge, this is the first study to establish SLP2 as a modulator of cristae structure. The observed decrease in CJ numbers and the accumulation of cristae stacks in *SLP2* KO resembles the defects found in MICOS KO models. In an attempt to elucidate whether the observed cristae defects in *SLP2* KO cells were primarily due to the decreased levels of MIC26, we tried to restore MIC26 expression in *SLP2* KO cells. Despite multiple trials, we were unable to generate *SLP2* KO with stable MIC26 overexpression. Consequently, to assess the similarity in cristae morphology defects, we compared *SLP2* KO cells with *MIC26* KO cells. While *MIC26* KO cells displayed slight cristae branching, there was no significant change in the number of cristae and CJs compared to WT (Figures 3D and 3E). The severity of cristae defects and the reduction in cristae and CJs numbers in *SLP2* KO cells exceeded those observed in *MIC26* KO cells. This indicates that the cristae defects in *SLP2* KO do not solely arise from the loss of MIC26. Instead, it implies an additional role of SLP2 in MICOS assembly and cristae morphology, distinct from its function in preserving MIC26 stability via YME1L regulation.

To further delineate the roles of SLP2 within MICOS assembly, we investigated whether SLP2 is necessary to facilitate the interaction between MIC13 and other MICOS components. We generated a double knockout model lacking both SLP2 and MIC13 (*MIC13-SLP2* DKO) and overexpressed MIC13-FLAG to examine how MIC13-FLAG interacts with MICOS subunits in the presence or absence of SLP2 (Figure S4). MIC13 was able to interact with all MICOS subunits even upon loss of SLP2, although the interaction with MIC26 was reduced due to MIC26 degradation in *SLP2* KO. This suggests that the interactions between MIC13 and MICOS subunits are independent of SLP2. Unexpectedly, while YME1L was initially employed as a control in our experiment, our findings revealed a specific interaction between YME1L and MIC13 that occurred independently of SLP2. This interaction had not been previously documented, adding a new layer to our understanding of MIC13's role within the MICOS complex.

Given that SLP2 is involved in SIMH, we investigated whether the interaction between SLP2 and MICOS affects SIMH. We assessed mitochondrial morphology in single knockout (KO) cell lines as well as in cells lacking both MIC13 and SLP2 (*MIC13-SLP2* DKO). To induce SIMH, we inhibited protein synthesis with cycloheximide and monitored mitochondrial morphology over time. We observed the accumulation of hyperfused mitochondria in WT cells within 2 h of treatment (Figures 3F and 3G). As expected, *SLP2* KO cells showed no response to SIMH induction as evidenced by quantification of mitochondrial morphology (Figure 3G). Interestingly, *MIC13* KO cells displayed hyperfusion similar to WT cells, while *MIC13-SLP2* DKO cells mirrored the response seen in the single *SLP2* KO (Figures 3F and 3G). This suggests that MIC13 is not implicated in the SLP2-mediated SIMH.

SLP2 and MIC13 synergistically contribute to the assembly and organization of the MIC60-subcomplex

During the evaluation of mitochondrial morphology in SIMH experiments, one of the interesting observations was that *MIC13-SLP2* DKO displayed a remarkably higher mitochondrial fragmentation compared to either of the single KOs (Figures 3F and 3G), even without treatment, underscoring the heightened impact of DKO of *SLP2* and *MIC13* on mitochondrial morphology. While mitochondrial morphology serves as a broad indicator of cellular fitness and stress, there could also be potential association between mitochondrial morphology and MICOS defects, for example deficiencies of MIC19 and MIC60 have been linked to altered mitochondrial morphology.[22,38] This promoted us to investigate any synergistic roles of MIC13 and SLP2 in MICOS assembly and cristae formation. To address this, we analyzed the steady state levels of individual subunits and complexes of MICOS in *MIC13-SLP2* DKO cells. While the steady state levels of MICOS subunits remained comparable between single *MIC13* KO and *MIC13-SLP2* DKO, the MIC26 levels appeared even more reduced in *MIC13-SLP2* DKO as compared to either single KO cells (Figure 4A). Strikingly, the assembly of MIC60 into the MICOS complex was significantly reduced in *MIC13-SLP2* DKO cells compared to *MIC13* KO (Figures 4B and 4C). Notably, MICOS complex in a native gel set-up runs as a smear with high intensity bands at two distinct sizes. In *MIC13* KO, the MICOS complex showed incomplete assembly, running at a reduced size due to loss of the MIC10-subcomplex as evidenced by BN-PAGE probed with MIC60 antibody (Figure 4B). We consistently found that the overall intensity of MIC60 in the MICOS complexes was considerably reduced, while the intensity of the OXPHOS complexes appeared unchanged in *MIC13-SLP2* DKO. This was quantitatively validated using densitometry analysis (Figure 4C), confirming that the MIC60 incorporation in the MICOS complex is reduced upon the simultaneous loss of *SLP2* and *MIC13*. This suggests that the absence of SLP2 in a *MIC13 KO* scenario hampers the assembly of MIC60 into MICOS complex, demonstrating a synergistic effect between SLP2 and MIC13 in promoting MIC60 assembly.

Our findings revealed a reduction in incorporation of MIC60 into the MICOS complex in *MIC13-SLP2* DKO cells, despite the steady state levels of MIC60 being comparable to controls (Figure 4A), suggesting that there might be a pool of MIC60 in the IM that is not the part of the MICOS complex. This promoted us to investigate the nanoscale distribution of MIC60 in the IM, using stimulated emission depletion (STED) SR nanoscopy, with MIC60 antibody. Previous studies have shown that MIC60 forms distinct punctate structures in IM, characterized by a

(E) Cristae number and CJs per mitochondrial section quantified from TEM images. Statistical analysis was performed using Student's *t* test. **p*-value $\leq$0.05, ***p*-value $\leq$0.01, *****p*-value $\leq$0.0001, ns = non-significant, *p*-value >0.05.
(F) Assessment of mitochondrial morphologies from WT, *MIC13* KO, *SLP2* KO and *MIC13-SLP2* DKO cells untreated or post treatment with 10 μM cycloheximide for 2 h. Scale bar represented as 15 μm.
(G) Percentage of cells displaying tubular, intermediate, fragmented or hyperfused mitochondria (*n* = 3). Statistical analysis was performed using Student's *t* test. ***p*-value $\leq$0.01, ****p*-value $\leq$0.001. Data represented as mean ± standard error of mean.

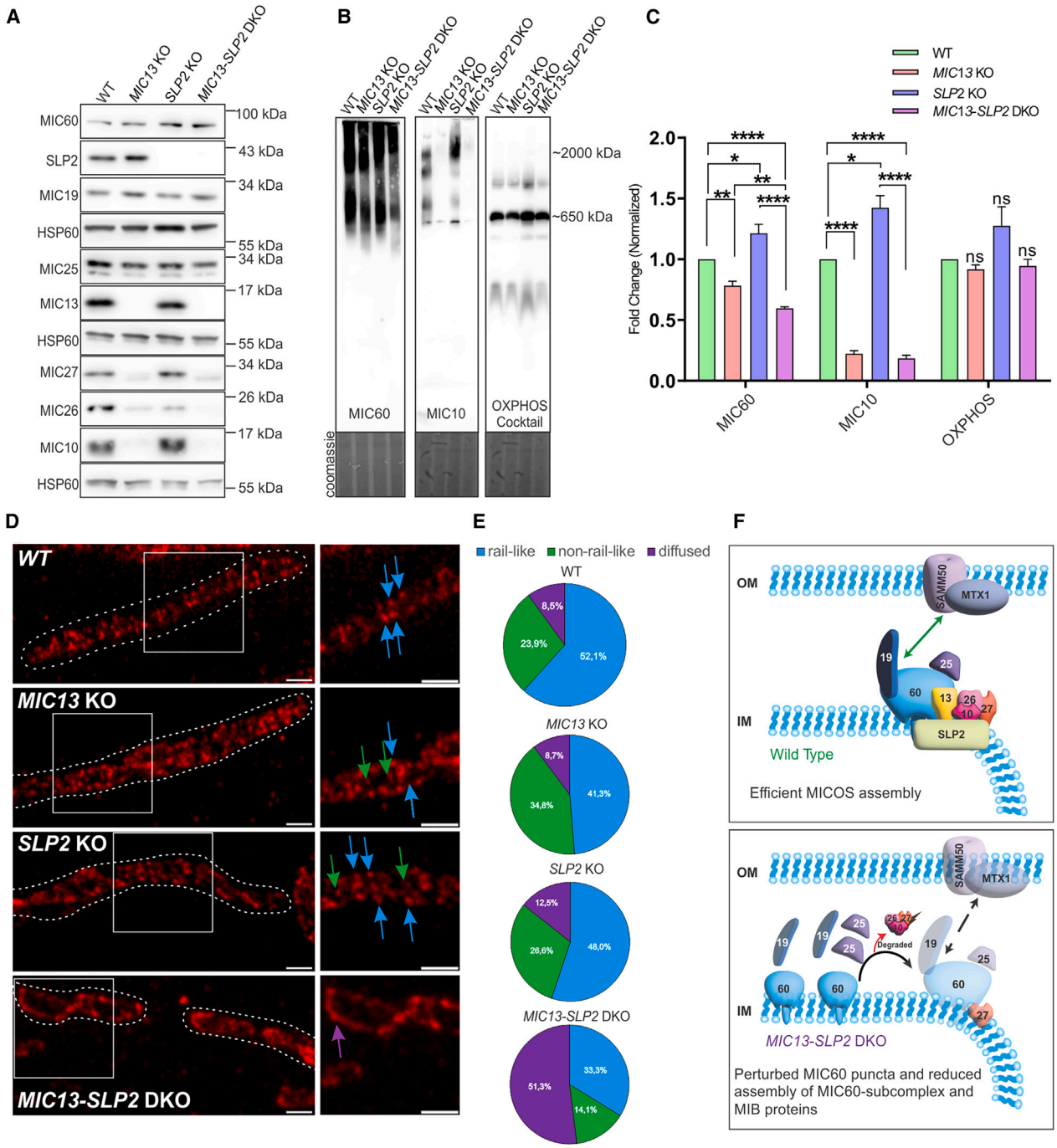

Figure 4. SLP2 and MIC13 synergistically modulate assembly and nanoscale distribution of MIC60

(A) Assessment of steady state levels of MICOS proteins with western blot from WT, *MIC13* KO, *SLP2* KO and *MIC13-SLP2* DKO cells. HSP60 serves as a loading control.

(B) BN-PAGE of isolated mitochondria from WT, *MIC13* KO, *SLP2* KO and *MIC13-SLP2* DKO cells to assess MICOS assembly. *MIC13-SLP2* DKO showed reduced MIC60 assembly in MICOS complex compared to any single KO. OXPHOS cocktail antibody is used as a control in BN-PAGE.

(C) BN-PAGE quantification depicting relative protein assembly levels normalized to Coomassie. Normalized intensities of MIC60 antibody signal throughout gel were used to calculate fold change relative to WT. Data is represented as mean ± standard error of mean, MIC60 ($n = 5$), MIC10 ($n = 4$), OXPHOS ($n = 3$). Statistical analysis was performed using Student's *t* test. *p-value ≤0.05, **p-value ≤0.01, ***p-value ≤0.001, ****p-value ≤0.0001, ns = non-significant, p-value >0.05.

(D) STED nanoscopy images from WT, *MIC13* KO, *SLP2* KO and *MIC13-SLP2 DKO* cells displaying MIC60 punctae. Images on the left side show individual mitochondria that are delineated by dotted lines. Images on the right-side zooms into the boxed mitochondria region. Blue arrows indicate individual MIC60 punctae in a rail-like arrangement in WT cells. Green arrow represents perturbed MIC60 puncta in *MIC13* KO and *SLP2* KO that are not arranged in rail-like

(legend continued on next page)

coordinated distribution pattern and rail-like arrangement along opposing sides of mitochondria.[9,39,40] In accordance with these studies, MIC60 displayed a punctate pattern with the rail-like arrangement in control cells (Figure 4D). This pattern of MIC60 staining resembles the arrangement of CJs in the mitochondria. However, MIC60 staining in the *MIC13-SLP2* DKO was remarkably different and disturbed compared to the WT cells and single KOs, with fewer punctate structures and patches where the staining was more evenly spread or diffused along the inner boundary membrane (IBM) (Figure 4D). The staining of MIC60 in single *MIC13* KO and *SLP2* KO cells was also perturbed with the rail-like pattern being less prominent as some MIC60 spots were also seen inside the mitochondria and not only on the edges (Figure 4D). It is plausible that MIC60 is present on the inner cristae stacks that are accumulated in *MIC13* KO and *SLP2* KO. We quantified this phenotype by analysing the percentage of mitochondria exhibiting different kind of MIC60 punctate patterns in these cell lines using a double-blind approach to ensure unbiased results (Figure 4E). Overall, we show that the combined loss of *SLP2* and *MIC13* was detrimental to MIC60 puncta organization, demonstrating the critical roles of SLP2 and MIC13 in orchestrating MIC60 arrangement and assembly (Figure 4F).

Given the crucial role of MIC60 as an anchor in formation of both MIC60-subcomplex and MIB complex, we analyzed MIC19, another component of MIC60-subcomplex, along with MIB components, SAMM50 and MTX1 using BN-PAGE. All these components exhibited reduced assembly in *MIC13-SLP2* DKO compared to either single KOs (Figure S5). This shows that the loss of MIC60 assembly or arrangement further impairs the assembly of the MIC60-subcomplex as well as the MIB complex, impacting MICOS-MIB assembly and emphasizing the synergistic role of SLP2 and MIC13 in mediating the assembly of the MICOS-MIB complex (Figure 4F).

To discern whether the loss of MIC60 assembly in *MIC13-SLP2* DKO arises from the absence of MICOS subunits or if it is a specific function of SLP2 and MIC13, we employed *MIC10* KO as a comparative element. *MIC10* KO cells exhibit a similar loss of MICOS subunits as seen in *MIC13-SLP2* DKO cells (Figures S1B and 3A). Interestingly, despite the comparable loss of MICOS subunits, *MIC10* KO did not impact MIC60 assembly (Figure S6). This observation suggests that the deficiency in MIC60 assembly observed in *MIC13-SLP2* DKO cells is not solely attributed to the loss of MICOS subunits alone. Instead, it highlights the unique collaborative function of SLP2 and MIC13 in regulating MIC60-subcomplex and MIB assembly.

SLP2 selectively regulates the assembly kinetics of MIC60-subcomplex

One of the questions that intrigued us was the role of SLP2 itself in the MICOS assembly, particularly as we were unable to earlier detect any apparent change in MIC60 assembly in the single *SLP2* KO (Figure S3). This lack of observable changes in *SLP2* KO may be attributed to compensatory effects that mask the underlying impact due to long-term depletion of a protein and/or due to its involvement in the transient assembly modes. Therefore, to dissect the mechanistic role of SLP2 in MIC60 assembly, we decided to analyze the kinetics of MICOS assembly and employed the Tet-On system that allow inducible and controlled gene expression over short timescales. We reintroduced MIC13 in *MIC13* KO (serving as control) and *MIC13-SLP2* DKO in a time-dependent manner and analyzed the re-assembly kinetics of the subunits of the MICOS complexes. For this, we generated pLIX403-MIC13-FLAG and stably expressed it in the *MIC13* KO and *MIC13-SLP2* DKO using the lentiviral transduction method. The addition of doxycycline initiates the expression of MIC13-FLAG in a time-dependent manner. After 8 h of doxycycline induction, MIC13-FLAG started to express in both *MIC13* KO and *MIC13-SLP2* DKO (Figure 5A). MIC13-FLAG was gradually expressed and incorporated into the MICOS complex of both *MIC13* KO and *MIC13-SLP2* DKO cells as seen by BN-PAGE at different time points after induction of protein expression (Figure 5B). Both MIC10 and MIC27 also progressively assembled in the MICOS complex over time (Figure 5C). The emergence of the MIC10-subcomplex, as indicated by MIC10 or MIC27, exhibited a more rapid and efficient kinetics in *MIC13-SLP2* DKO cells compared to the *MIC13* KO cells. This could be attributed to a slightly higher expression of MIC13-FLAG in *MIC13-SLP2* DKO compared to the *MIC13* KO, potentially due to differential integration of the overexpressed cassette. On the contrary, the incorporation of MIC60 into the MICOS complex was slower in *MIC13-SLP2* DKO cells compared to the *MIC13* KO after expression of MIC13-FLAG (Figure 5C). This observation was corroborated quantitatively through densitometry analysis of MIC60 at the 8-h' time point in different cell lines (Figure 5D). This delay in MIC60 assembly was further confirmed through extended time points (up to 48 h) (Figures S7A and S7B), consistently showing that absence of SLP2 hampers the assembly of MIC60. Despite the presence of the already assembled MIC10-subcomplex, the assembly of MIC60 into the MICOS complex was notably delayed in the absence of SLP2. Thus, it is evident that the assembly kinetics of the MIC60-subcomplex, rather than the MIC10-subcomplex, is dependent on SLP2 (Figures 5C and 5D), highlighting the specific regulatory role of SLP2 in facilitating the incorporation of MIC60 into the MICOS complex upon gradual restoration of MIC13 (Figure 5E).

Stabilized MIC10 facilitates seeding of MIC60 and crista junction formation

Understanding the specific role of MIC13 in stabilizing MIC10, we wanted to ask how stabilizing the MIC10-subcomplex might impact the formation of the MIC60-subcomplex in *MIC13-SLP2* DKO cells. To achieve this, we depleted YME1L in *MIC13-SLP2 DKO* cells, thereby stabilizing the MIC10-subcomplex

arrangement. Purple arrow shows evenly spread (diffuse) MIC60 puncta in *MIC13-SLP2* DKO cells suggesting an altered pattern compared to WT. Scale bars represent the 500 nm.

(E) Percentage of individual mitochondria displaying MIC60 puncta predominately arranged as rail-like pattern, non-rail-like pattern, or diffuse pattern is presented in a pie-chart format.

(F) A model depicting that MIC60-subcomplex and MIB assembly is dependent on SLP2-MIC13.

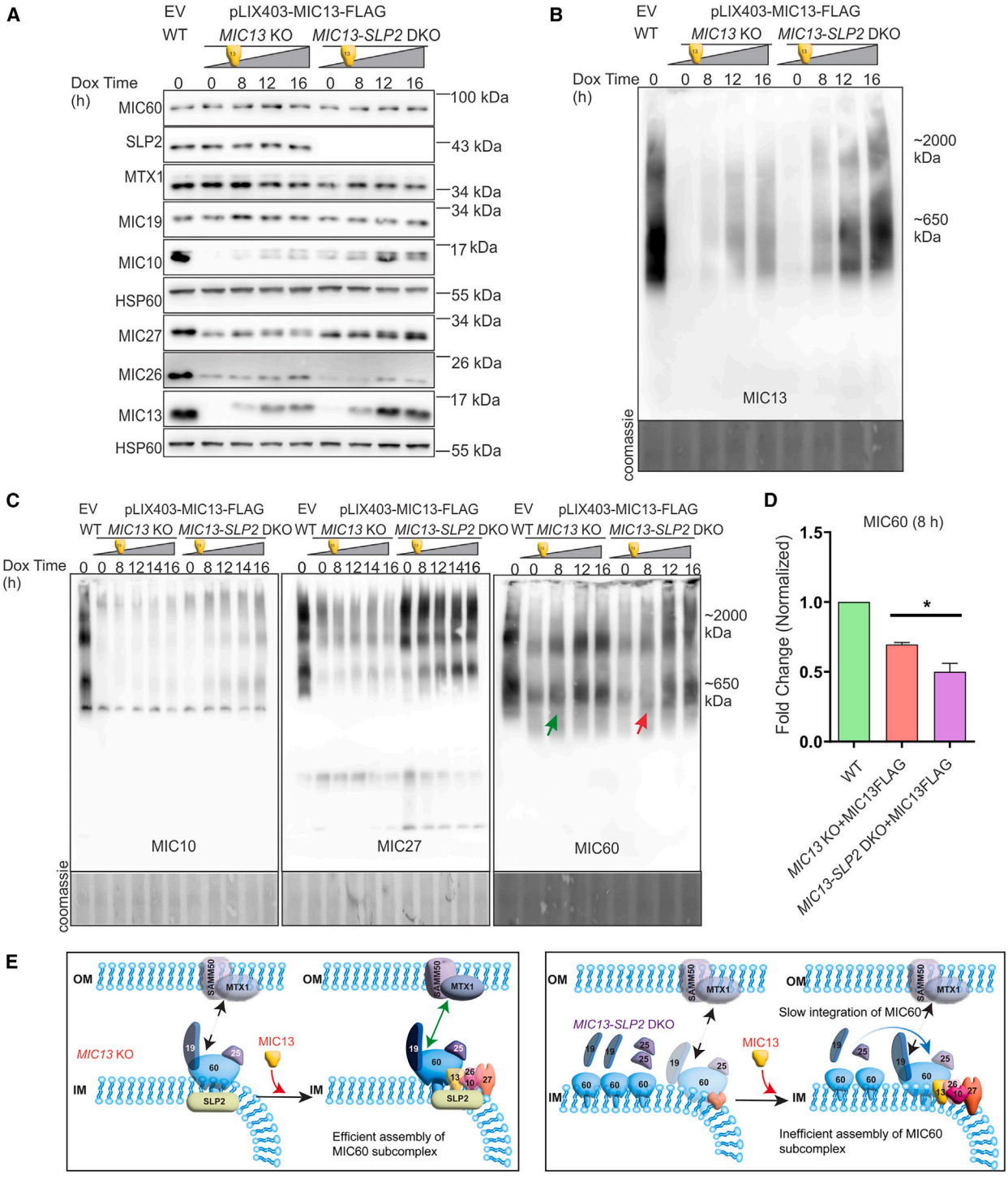

Figure 5. SLP2 specifically regulates assembly kinetics of MIC60

(A) WT cells stably expressing pLIX403 EV and *MIC13* KO, *MIC13-SLP2* DKO cells stably expressing pLIX403-MIC13-FLAG were treated with 1 μg/mL of doxycycline (Dox) for indicated time points and western blot analysis depicting steady state levels of MICOS proteins upon induction of MIC13-FLAG are shown. HSP60 serves as a loading control.

(B) BN-PAGE with isolated mitochondria from WT cells stably expressing pLIX403 EV, and *MIC13* KO and *MIC13-SLP2 DKO* cells stably expressing pLIX403-MIC13-FLAG treated with 1 μg/mL of doxycycline (Dox) for indicated time points showing stable incorporation of MIC13-FLAG in MICOS complex.

(C) BN-PAGE with isolated mitochondria from WT cells stably expressing pLIX403 EV, and *MIC13* KO and *MIC13-SLP2 DKO* cells stably expressing pLIX403-MIC13-FLAG treated with 1 μg/mL of Dox for indicated time points was probed for MIC10, MIC27 and MIC60 antibody. The green arrow (in the *MIC13* KO lane)

(legend continued on next page)

(Figure 6A). Surprisingly, we observed a partial restoration in the assembly of MIC60 when MIC10 was stabilized through YME1L depletion in *MIC13-SLP2* DKO cells (Figures 6B and 6C), despite similar steady-state levels of MIC60 (Figure 6A). This observation is crucial as it suggests that MIC10, even in the absence of SLP2 or MIC13, can serve as a 'docking platform' facilitating the integration of MIC60 into the MICOS complex. Depletion of OMA1, another mitochondrial protease in the IM did not show a significant impact on steady-state levels of MICOS subunits (Figure S8). MICOS assembly has been assumed to follow a hierarchical step with MIC60 being the first component.[41] However, these findings challenge this notion and demonstrate an interdependence between the assembly of the MIC60 and MIC10-subcomplex. Especially, this highlights that the role of MIC13 in the MIC13-SLP2 interplay is to ensure the stability and assembly of MIC10-subcomplex. This assembled MIC10-subcomplex, along with SLP2, is crucial in seeding the assembly of MIC60 by providing an assembly platform. The partial restoration of MIC60 assembly also influences the assembly of MIC19 (Figure S9) and MIB complex protein MTX1 (Figure 6B) in *MIC13-SLP2* DKO cells depleted for YME1L. Based on these findings, we propose that the collaboration between SLP2 and the MIC10-subcomplex forms what we term the 'seeder' complex that plays a crucial role in facilitating the assembly of the MIC60-subcomplex. This highlights an interdependence between the assembly of the two MICOS subcomplexes, suggesting a coordinated rather than initially distinct assembly pathways for the two subcomplexes that merge at a later stage.

We delved into the next significant question regarding the impact of the proposed 'seeder' complex formation and MIC60 assembly on cristae morphology. To address this, we analyzed the mitochondrial ultrastructure in the single and DKO cell lines of *SLP2* and *MIC13* with or without the depletion of YME1L. *MIC13* KO displayed cristae stacks or concentric cristae, while *SLP2* KO displayed a stack-like cristae albeit with more swollen cristae (Figures 1D, 3D, and 6D). Extensive quantification of EM images corroborated these findings, showing significant reduction in the number of cristae and CJs in both single KOs (Figures 6D and 6E), reminiscent of defects typically associated with MICOS KO (Figures 1D and 1E). *MIC13-SLP2* DKO cells exhibited a severe phenotype similar to *MIC13* KO cells, with a substantial decrease in the numbers of cristae and CJs. OPA1 loss can cause cristae defects; however, no apparent changes in OPA1 levels or processing were observed in these cell lines, indicating that the defects do not result from altered OPA1 (Figure S10). The depletion of YME1L restored cristae and CJs in both *MIC13* KO and *MIC13-SLP2* DKO cells (Figures 6D and 6E, 1D), in alignment with significant contribution of MIC10-subcomplex in cristae and CJ formation in these scenarios. Depletion of YME1L in *SLP2* KO visibly reduced cristae swelling. While swelling of cristae is not typically observed in MICOS KOs, it is likely that the swelling in *SLP2* KO arises from another unknown substrate regulated by SLP2-YME1L. Our data confirm that SLP2 plays a vital role in MIC60 assembly, especially in the presence of MIC10-subcomplex. This supports its important role in cristae and CJ formation, as shown by the TEM images displaying a significant reduction in CJs and additional cristae swelling. Specially, the observed rescue in MIC60-subcomplex assembly and cristae phenotype upon stabilizing MIC10-subcomplex in *MIC13-SLP2* DKO cells further validates the 'seeder' hypothesis, adding a new layer toward understanding MICOS assembly, and its direct involvement in cristae and CJs formation.

DISCUSSION

In this study, we have addressed multiple known and previously unknown players regulating the interplay between the MIC10- and the MIC60-subcomplex allowing us to come up with an updated multi-step model for MICOS assembly which reveals unexpected insights and marks a significant shift in our understanding of MICOS assembly and cristae formation (Figure 7). Our findings highlight the special role of MIC13 in stabilizing MIC10-subcomplex rather than acting as a bridge. Interestingly, the MIC13-YME1L interaction can occur independently of SLP2, revealing the intricate regulation of MICOS stabilization by different pathways, partially dependent of SLP2. While SLP2 shields MIC26 from YME1L-mediated proteolysis, its function exceeds MIC26 stabilization, as it collaborates with MIC13 to regulate the kinetic assembly of MIC60 into the MICOS-MIB complex. Once stabilized, MIC10-subcomplex along with SLP2 forms what we term as the 'seeder' complex, facilitating the assembly of MIC60-subcomplex and MIB within the MICOS-MIB complex (Figure 7). Combined depletion of MIC13 and SLP2 disrupts MIC60's nanoscale distribution and its incorporation into MICOS complex. We suggest that the 'seeder' complex promotes the nanoscale punctate distribution of MIC60 and assembly of MIC60, culminating in the formation of MICOS-MIB complex. Subsequently, the 'seeder' complex, thereby facilitating MIC60-subcomplex assembly, contributes to the formation of nascent CJs (Figure 7). In addition to identifying SLP2 as a regulator of cristae morphology, our model highlights several key insights. These include the identification of intricate and partially overlapping quality control pathways in MICOS regulation, the elucidation of specific functions of MIC13, and the recognition of the interdependence between the MIC10- and MIC60-subcomplexes in the assembly of the MICOS-MIB complex.

MIC13, an integral component of the mitochondrial IM, plays a vital role in cristae morphogenesis and loss of MIC13 results in severe mitochondrial hepato-encephalopathy. Although previous research has extensively detailed the consequences

and red arrow (in the *MIC13-SLP2 DKO* lane) highlight the delay in assembly of MIC60 at the 8-h timepoint. The assembly kinetics of the MIC60-subcomplex, rather than the MIC10-subcomplex, is dependent on SLP2.

(D) BN-PAGE quantification depicting relative protein assembly levels of MIC60 at 8 h normalized to Coomassie. Normalized intensities of MIC60 antibody signal throughout gel were used to calculate fold change relative to WT. Data is represented as mean ± standard error of mean ($n = 3$). The quantification reveals delayed MIC60 assembly in the absence of SLP2. Statistical analysis was performed using Student's t test. *p-value ≤ 0.05.

(E) A model depicting the assembly kinetics of MIC60 in MICOS complex depends on SLP2. Slower incorporation of MIC60 is observed in the absence of SLP2 upon reintroduction of MIC13 in *MIC13-SLP2 DKO*.

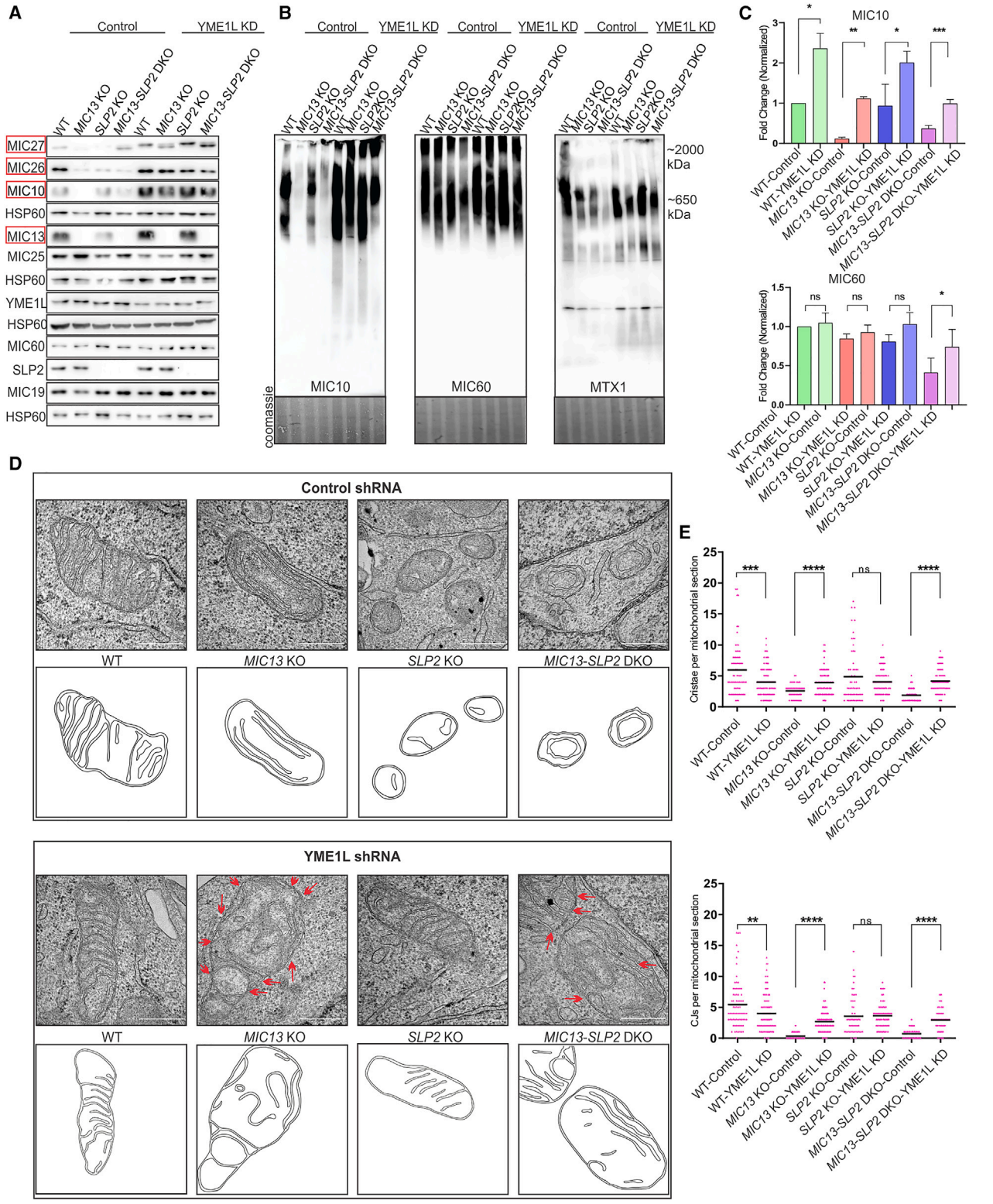

Figure 6. Stabilized MIC10-subcomplex for MIC60 seeding and CJ formation

(A) Western blot analysis of WT, *MIC13* KO, *SLP2* KO, *MIC13-SLP2* DKO stably expressing pGIPZ-Control shRNA or pGIPZ-YME1L shRNA (KD) to assess steady state levels of MICOS proteins. The steady state levels of MIC60 remain unaltered across different cell lines. HSP60 serves as a loading control.

(legend continued on next page)

of MIC13 depletion, the underlying molecular mechanisms leading to the phenotypes are largely unknown. The challenge arises in distinguishing the specific function of MIC13 from other MIC10-subcomplex proteins due to the concurrent loss of the MIC10-subcomplex in *MIC13* KO. Interestingly, upon depleting YME1L in *MIC13* KO, the MIC10-subcomplex could be restored, providing a unique scenario to study the specific role of MIC13. To our surprise, the restored MIC10-subcomplex exhibited the ability to interact with the MIC60-subcomplex even in the absence of MIC13. This finding shows that MIC13 is primarily required for MIC10 stability rather than serving as an essential bridging component. The presence of nascent CJs upon restoration of MIC10 in *MIC13* KO showed that the assembled MIC10-subcomplex could form CJs even in the absence of MIC13. MIC10 is known to oligomerize in a wedge-like shape that causes membrane bending and CJ formation.[10,11] However, it remains to be answered whether this CJ restoration is sufficient to address MIC13-specific mitochondrial defects or the associated pathology. In addition to maintaining MIC10 stability, we observed that MIC13 exclusively influences the status of MIC27, resulting in a lower molecular weight variant. Although the identity of this MIC27 variant remains unknown, its specificity to MIC13 suggests that MIC13 may have additional specialized roles critical for its function and associated pathology. In conclusion, we remain optimistic that future studies will further elucidate whether restoration of MIC10 serves as a tool to determine the mechanisms underlying MIC13-associated diseases and holds promise for the development of future therapeutics.

Employing a co-IP coupled MS approach, we discovered SLP2 as an interactor of MIC13, revealing a previously unknown multi-layered role of SLP2 in maintaining MICOS assembly and cristae formation. To the best of our knowledge, no prior studies have identified SLP2 as a cristae modulator or explored the mechanism through which SLP2 regulates cristae formation. Our study comprehensively illustrates the role of SLP2 in MICOS assembly and cristae formation, substantiated by the following results: (1) Using KOs models of individual MICOS subunits and stable overexpression cell lines, we determined that SLP2 not only interacts with MIC13 but also with each MICOS subunit, forming a large interaction hub of SLP2-MICOS in the mitochondrial IM. (2) Depletion of SLP2 resulted in pronounced cristae defects, including swollen cristae and reduced number of cristae and CJs, with the later resembling the defects observed in MICOS KO models. (3) SLP2 is essential for preserving the stability of MIC26 by regulating YME1L-mediated proteolysis. However, the cristae defects in *SLP2* KO were substantially more severe compared to *MIC26* KO pointing toward the broader role of SLP2 in MICOS assembly and cristae formation. (4) The DKO of *MIC13* and *SLP2* exhibited additive defects, particularly in MIC60-subcomplex and MIB assembly into the MICOS complex, leading to perturbed nanoscale arrangement of MIC60 punctae in the IM. This suggests a synergistic role of SLP2 and MIC13 in facilitating the formation of MIC60 puncta and its incorporation into the MICOS complex. (5) The time-dependent restoration of MIC13 in *MIC13-SLP2* DKO cells showed a considerably slower kinetics of the assembly of MIC60 into MICOS complex compared to *MIC13* KO, demonstrating a critical role of SLP2 in specifically regulating MIC60 assembly kinetics. (6) Interestingly, the restoration of MIC10-subcomplex in simultaneous depletion of *SLP2* and *MIC13* could restore MIC60 assembly and lead to formation of nascent CJs. By combining these findings, we introduce SLP2 as a cristae modulator, specifically assisting MIC60-subcomplex and MIB assembly and facilitating cristae organization.

We further clarified the specific roles of MIC13 and found that, fundamentally, MIC13 is not essential for bridging MIC10- and MIC60-subcomplexes, instead its crucial function lies in shielding the MIC10-subcomplex by protecting it from YME1L-mediated proteolysis. Instead of relying on an overexpression strategy, we employed a unique approach of stabilizing MIC10-subcomplex with YME1L depletion in *MIC13* KO as a means to support and validate our model. This approach not only serves as a tool for validation but also offers additional insights into the mechanisms underlying MIC13-mediated pathology. We observed that the restoration of MIC10 not only partially recovered the MIC60 assembly in the *MIC13-SLP2* DKOs, but also prompted the re-formation of nascent CJs. This emphasizes the mutual interdependence of SLP2 and MIC13, particularly in stabilizing MIC10-subcomplex, for the MICOS assembly and the formation of cristae and CJs. Combining our data, which shows the absence of SLP2 delays the assembly of MIC60 and alterations of MIC60 foci formation in *MIC13-SLP2* DKOs, we suggest that the combined actions of SLP2 and MIC10-subcomplex act as a seeding mechanism for the incorporation of MIC60-subcomplex into the MICOS complex (Figure 7C), thereby, leading to formation of MICOS-MIB complex and further promoting cristae and CJ morphogenesis. The MIC10-subcomplex serves as a docking platform for further assembly of MIC60-subcomplex into the MICOS complex, illustrating an interdependence between MIC60- and MIC10-subcomplex during the formation

(B) BN-PAGE with isolated mitochondria from WT, *MIC13* KO, *SLP2* KO, *MIC13-SLP2* DKO stably expressing pGIPZ-Control shRNA or pGIPZ- YME1L shRNA. The stabilized MIC10-subcomplex upon YME1L depletion could partially rescue the incorporation of MIC60 and MTX assembly in *MIC13-SLP2* DKO. This shows that MIC10-subcomplex provides a docking site for assembly of MIC60.

(C) BN-PAGE quantification depicting relative protein assembly levels normalized to Coomassie. Normalized intensities of MIC60 antibody signal throughout gel were used to calculate fold change relative to WT. Data is represented as mean ± standard error of mean (n = 3). Statistical analysis was performed using Student's t test. *p-value ≤0.05, **p-value ≤0.01, ***p-value ≤0.001, ns = non-significant, p-value >0.05.

(D) Mitochondrial cristae morphology accessed using TEM from WT, *MIC13* KO, *SLP2* KO, *MIC13-SLP2* DKO stably expressing pGIPZ-Control shRNA or pGIPZ-YME1L shRNA. Scale bar represents 0.5 μm. The skeletonization of the TEM image is depicted below the image. Mitochondria in *MIC13* KO, *SLP2* KO, *MIC13-SLP2* DKO display loss of cristae and CJs, with cristae arranged as either stacks or concentric rings. *SLP2* KO additionally display swollen cristae. YME1L depletion showed beneficial consequences on cristae morphology with presence of nascent CJs (red arrows). This shows that loss of CJs in *MIC13* KO is attributed to MIC10 loss, and swelling of *SLP2* KO cristae is visibly restored upon YME1L depletion.

(E) Quantification of crista and CJs per mitochondrial section. Outliers were removed with Grubbs' method and statistical significance was analyzed using Student's t test. *p-value ≤0.05, **p-value ≤0.01, ***p ≤ 0.001, ****p-value ≤0.0001, ns = non-significant, P-value >0.05.

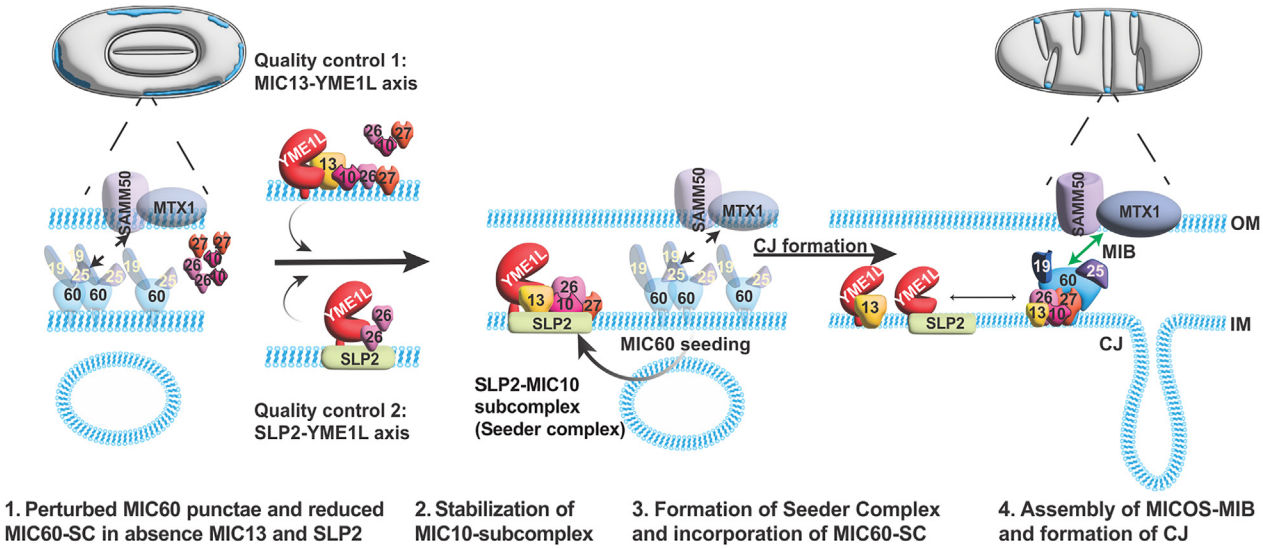

Figure 7. Schematic illustration of synergistic role of SLP2 and MIC13 in MICOS assembly and crista junction formation

The schematic model illustrates the quality control processes involved in cristae junction (CJ) morphogenesis and MICOS homeostasis, mediated by the MIC13-YME1L and SLP2-YME1L, which differentially stabilize components of the MIC10-subcomplex. This process facilitates the formation of the "seeder complex", which consists of SLP2 and the stabilized MIC10-subcomplex. The simultaneous depletion of *MIC13* and *SLP2* disrupts the nanoscale distribution of MIC60 and its integration into the MICOS complex. The proposed "seeder model" suggests that the formation of the seeder complex is crucial for organizing the punctate distribution of MIC60 and facilitating its assembly into the MICOS-MIB complex. This process is essential for the formation of nascent CJs and establishing contact sites between IM and OM. In addition to identifying SLP2 as a regulator of cristae morphology, this model provides key insights into the intricate and partially overlapping quality control pathways governing MICOS regulation, elucidates specific functions attributed to MIC13, and highlights the interdependency between the MIC10- and MIC60-subcomplexes in MICOS-MIB complex assembly.

of the MICOS complex. The concomitant reappearance of CJs upon stabilization of MIC10-subcomplex provides mechanistic insights for formation of nascent CJs. In summary, our study not only refines the model for MICOS assembly but also offers valuable insights into the intricate processes underlying the formation of cristae and CJs.

SLP2, a member of the SPFH superfamily, performs diverse roles in mitochondrial functions, involving mitochondrial dynamics during stress, quality control and cell survival.[34,35] It binds to cardiolipin to regulate mitochondrial biogenesis.[33] Moreover, it serves as an anchor for a proteolytic hub in mitochondria called SPY complex regulating proteases such as YME1L and PARL.[35] In our study, we show using several lines of evidences that SLP2 act as a scaffold, forming a large interaction hub within the IM with all the subunits of MICOS complex. While this manuscript focuses on understanding the MIC13-SLP2 synergy in MIC60 assembly, our data suggest that SLP2 may have a broader role in cristae morphogenesis. This direct regulation of MICOS assembly and cristae formation prompts the question how SLP2 performs these tasks in the mitochondria, specifically in the context of cristae formation. While the regulation of MIC26 by SLP2 can be explained by the SLP2-YME1L interaction, introducing MIC26 as a player that is influenced by the SPY complex, understanding how SLP2 influences the seeding of MIC60-subcomplex assembly and its docking with MIC10-subcomplex remains a challenge. It is well possible that SLP2 generates a suitable lipid microenvironment facilitating MIC60 punctae formation, possibly through direct interaction or cardiolipin recruitment. Moreover, SLP2-delineated lipid domains, enriched in cardiolipin, could directly or indirectly impact cristae formation and MIC60 assembly. Furthermore, we cannot exclude the presence of an unknown substrate of YME1L under regulation of SLP2, whose absence contributes toward cristae swelling and identification of this protein could broaden our understanding of its role in cristae morphogenesis. Addressing these complexities requires challenging experiments aimed at elucidating the lipid microenvironment of SLP2, providing crucial insights into how SLP2 contributes to the MICOS assembly and cristae formation.

The changed kinetics were crucial in revealing the regulatory role of SLP2 in MICOS assembly. It is important to note that MIC13 levels were elevated from the start in *MIC13-SLP2* KO cells. While multiple lines of evidences showed that *MIC13-SLP2* KO directly impacts MIC60 assembly, we cannot entirely exclude the possibility that higher MIC13 levels might additionally contribute to delayed MIC60 assembly observed in these experiments. Moreover, since *SLP2* KO primarily affects the kinetics of MIC60 assembly, we believe that this regulation may become particularly important under conditions where mitochondrial function or cristae morphogenesis is critical, such as during intense exercise, aging, or mitochondrial diseases. Therefore, it would be valuable to investigate further how the SLP2-MICOS interaction regulates cristae morphology during states of increased energy demand, where cristae biogenesis or morphogenesis is upregulated. This line of research could offer key insights into how mitochondria adapt to physiological stress and pathological conditions.

We demonstrate that MIC26 is a YME1L substrate, specifically regulated by SLP2-YME1L. We recently reported a pathogenic *MIC26* mutation causing lethal mitochondrial disease with progeria-like phenotypes.[31] This C-terminal truncated MIC26 variant is prone to faster degradation, behaving like a loss-of-function variant. *MIC26* mutations were also associated with recessive mitochondrial myopathy, lactic acidosis, cognitive impairment and autistic features.[42] Exploring degradation pathways of MIC26 in these pathological scenarios could offer insights into underlying patho-mechanisms in MIC26-associated pathologies.

MICOS contains several subunits, each contributing uniquely in maintaining mitochondrial structural integrity, subdivided into two subcomplexes, MIC60-subcomplex and MIC10-subcomplex. Several previous studies have elucidated the distinct function of each subcomplex, collectively contributing to overall functionality of MICOS. While the MIC60-subcomplex is responsible to connect IM and OM and shape CJs, MIC10-subcomplex controls lamellar cristae biogenesis and promotes CJ formation.[8,11,43] It was believed that MICOS assembly followed a hierarchical order, with the assembly of the MIC60-subcomplex preceding that of the MIC10-subcomplex. MIC60 was considered a master regulator in this assembly process.[41,44] However, our results reveal an intricate interdependence between these two subcomplexes, wherein the kinetics of MICOS subcomplexes assembly progresses in a mutually interdependent manner. This interdependence between the two MICOS subcomplexes ensures the quality of MICOS assembly, preventing the formation of futile subcomplexes unless the assembly can be completed. Our findings highlight a more integrated and coordinated assembly process in which SLP2 emerges as a key player in facilitating this process.

Our data also highlights the delicate balance between the regulation of mitochondrial proteases, specifically YME1L, and the integrity of MICOS assembly and mitochondrial cristae. While SLP2 protects MIC26 from YME1L-mediated proteolysis, we observed MIC13 interacting with YME1L independently of SLP2. The functional significance of this MIC13-YME1L interaction remains elusive, prompting future investigations to elucidate whether MIC13 directly influences YME1L activity or whether YME1L plays an indirect role during stress conditions induced by the deletion of MICOS subunits. Previous studies have implicated mitochondrial proteases in the control of cristae morphology, highlighting the broader impact of quality control pathways on the safety and integrity of mitochondrial membrane structures. MIC60 and SAMM50 were also shown to be proteolytic substrates of YME1L during *MIC19* downregulation[22,38] showing the complexity of regulation of MICOS assembly. Additionally, OMA1, another IM protease also associated with the MICOS complex[45] and proteolytically regulated MIC19 assembly in the MIB complex.[22] Overall, our study deciphers a unique quality control mechanism governing MICOS and MIB assembly, advancing our understanding of the factors orchestrating cristae morphogenesis.

The precise mechanisms underlying the formation and function of CJs and contact sites remain incompletely understood. The MICOS subunits have been implicated in several important cellular functions including the import of mitochondrial proteins, biogenesis and transfer of phospholipids, mtDNA organization, apoptosis, mitophagy, mitochondrial transport, mitochondrial translation, mitochondrial morphology, and inflammation.[6,46] Exploring the role of SLP2 holds promise for providing new insights into many of these cellular processes. Future studies investigating these components and their interactions may reveal mechanisms into the intricate regulation of mitochondrial ultrastructure and its impact on broader cellular pathways.

Limitations of the study

While this study offers valuable insights into the role of MIC13-SLP2 in regulating MICOS assembly and cristae morphogenesis, a few limitations need further exploration. The functional interactions between SLP2, MIC13, and YME1L, particularly in relation to MICOS assembly and cristae morphogenesis, remain incompletely understood. While SLP2 seems to influence the MIC60-subcomplex, whether it directly interacts with MIC60 or works through cardiolipin recruitment remains speculative and requires more research. How SLP2 interacts with other MICOS subunits is not yet fully understood. The potential involvement of an unidentified YME1L substrate, regulated by SLP2 and contributing to cristae morphology, particularly cristae swelling, represents another promising area for future research. Additionally, while *SLP2* KO affects the kinetics of MIC60 assembly, the impact of elevated MIC13 levels on this process requires further clarification. *SLP2* KO alone does not impair MIC60 assembly, suggesting that studying the regulation of cristae morphology under conditions of high energy demand, such as during exercise or mitochondrial disease, may help uncover the physiological role of SLP2 in cristae dynamics. Moreover, the study is limited in understanding the specific functions of MIC13 beyond its relationship with MIC10, as many defects can be rescued by restoring MIC10 levels. Whether this rescue is sufficient to mitigate disease conditions or restore disease phenotypes remains unknown and presents a compelling avenue for further research.

RESOURCE AVAILABILITY

Lead contact

Requests for resources and reagents should be directed to and will be fulfilled by the lead contact, Ruchika Anand (anand@hhu.de).

Material availability

Plasmids and cell lines generated in this study are available from lead contact under a material transfer agreement with Heinrich-Heine University-Düsseldorf.

Data and code availability

- Data: The mass spectrometry proteomics data have been deposited to the ProteomeXchange Consortium via the PRIDE partner repository with the assigned Accession number (PRIDE: PXD044968), which is also provided in the key resources table. The data are publicly accessible as of the publication date.
- Code: This paper does not report original code.
- Additional Information: Any additional information required to reanalyze the data reported in this paper is available from lead contact upon request.

ACKNOWLEDGMENTS

Authors would like to thank Andrea Borchardt, Tanja Portugall for their technical assistance in cloning and electron microscopy. We further thank Anny

Garces Palacio as student assistant for performing microscopy experiments. We thank Melissa Damiecki for help in skeletonization of TEM images. Electron microscopy was performed at the Core facility for electron microscopy (CFEM) at the medical faculty of the Heinrich Heine University Düsseldorf. The STED imaging experiments were performed at the Center for Advanced Imaging (CAi) at Heinrich Heine University Düsseldorf.The research was supported by funding from Medical faculty of Heinrich Heine University Düsseldorf, Foko-02/2015 (R.A. and A.S.R.), FoKo-2020-71 (R.A.), FoKo 2022-11 (A.K.K.) and Deutsche Forschungsgemeinschaft grant, AN 1440/3-1 (R.A.), AN 1440/4-1 (R.A.), KO 6519/1-1 (A.K.K.) and SFB 1208 project B12 (ID 267205415) to A.S.R.

AUTHOR CONTRIBUTIONS

R.N.: Investigation, methodology, data curation, formal analysis, visualization, writing—original draft, writing—review and editing. R.S.: Investigation, methodology, data curation, formal analysis. Y.S.: Investigation, methodology, data curation, formal analysis. J.U.: Investigation, methodology, formal analysis. I.W.: investigation, methodology, formal analysis, data curation. A.S.R.: supervision, funding acquisition, writing—review and editing. A.K.K.: formal analysis, supervision, validation, funding acquisition, writing—review and editing. R.A.: conceptualization, data curation, formal analysis, supervision, methodology, funding acquisition, project administration, writing—original draft, writing—review and editing.

DECLARATION OF INTERESTS

The authors declare no competing interests.

STAR★METHODS

Detailed methods are provided in the online version of this paper and include the following:

- KEY RESOURCES TABLE
- EXPERIMENTAL MODEL AND STUDY PARTICIPANT DETAILS
  - Cell lines and cell culture
- METHOD DETAILS
  - Co-immunoprecipitation coupled mass spectrometry
  - Proximity ligation assay
  - CRISPR-Cas9 knockout generation
  - Molecular cloning
  - Generation of stable cell lines and siRNA knockdown
  - SDS PAGE and western blot
  - Mitochondria isolation
  - Co-immunoprecipitation
  - Blue native gel electrophoresis (BN-PAGE)
  - Mitochondria morphology analysis
  - Stimulated emission depletion (STED) nanoscopy
  - Electron microscopy
- QUANTIFICATION AND STATISTICAL ANALYSIS

SUPPLEMENTAL INFORMATION

Supplemental information can be found online at https://doi.org/10.1016/j.isci.2024.111467.

Received: June 11, 2024
Revised: September 2, 2024
Accepted: November 21, 2024
Published: November 23, 2024

REFERENCES

1. Monzel, A.S., Enríquez, J.A., and Picard, M. (2023). Multifaceted mitochondria: moving mitochondrial science beyond function and dysfunction. Nat. Metab. *5*, 546–562. https://doi.org/10.1038/s42255-023-00783-1.
2. Perkins, G., Renken, C., Martone, M.E., Young, S.J., Ellisman, M., and Frey, T. (1997). Electron tomography of neuronal mitochondria: three-dimensional structure and organization of cristae and membrane contacts. J. Struct. Biol. *119*, 260–272. https://doi.org/10.1006/jsbi.1997.3885.
3. Mannella, C.A., Lederer, W.J., and Jafri, M.S. (2013). The connection between inner membrane topology and mitochondrial function. J. Mol. Cell. Cardiol. *62*, 51–57. https://doi.org/10.1016/j.yjmcc.2013.05.001.
4. Scorrano, L., Ashiya, M., Buttle, K., Weiler, S., Oakes, S.A., Mannella, C.A., and Korsmeyer, S.J. (2002). A distinct pathway remodels mitochondrial cristae and mobilizes cytochrome c during apoptosis. Dev. Cell *2*, 55–67. https://doi.org/10.1016/s1534-5807(01)00116-2.
5. Kondadi, A.K., and Reichert, A.S. (2024). Mitochondrial Dynamics at Different Levels: From Cristae Dynamics to Interorganellar Cross Talk. Annu. Rev. Biophys. *53*, 147–168. https://doi.org/10.1146/annurev-biophys-030822-020736.
6. Anand, R., Reichert, A.S., and Kondadi, A.K. (2021). Emerging Roles of the MICOS Complex in Cristae Dynamics and Biogenesis. Biology *10*, 600. https://doi.org/10.3390/biology10070600.
7. Mukherjee, I., Ghosh, M., and Meinecke, M. (2021). MICOS and the mitochondrial inner membrane morphology - when things get out of shape. FEBS Lett. *595*, 1159–1183. https://doi.org/10.1002/1873-3468.14089.
8. Stephan, T., Brüser, C., Deckers, M., Steyer, A.M., Balzarotti, F., Barbot, M., Behr, T.S., Heim, G., Hübner, W., Ilgen, P., et al. (2020). MICOS assembly controls mitochondrial inner membrane remodeling and crista junction redistribution to mediate cristae formation. EMBO J. *39*, e104105. https://doi.org/10.15252/embj.2019104105.
9. Kondadi, A.K., Anand, R., Hänsch, S., Urbach, J., Zobel, T., Wolf, D.M., Segawa, M., Liesa, M., Shirihai, O.S., Weidtkamp-Peters, S., and Reichert, A.S. (2020). Cristae undergo continuous cycles of membrane remodelling in a MICOS-dependent manner. EMBO Rep. *21*, e49776. https://doi.org/10.15252/embr.201949776.
10. Barbot, M., Jans, D.C., Schulz, C., Denkert, N., Kroppen, B., Hoppert, M., Jakobs, S., and Meinecke, M. (2015). Mic10 oligomerizes to bend mitochondrial inner membranes at cristae junctions. Cell Metabol. *21*, 756–763. https://doi.org/10.1016/j.cmet.2015.04.006.
11. Bohnert, M., Zerbes, R.M., Davies, K.M., Mühleip, A.W., Rampelt, H., Horvath, S.E., Boenke, T., Kram, A., Perschil, I., Veenhuis, M., et al. (2015). Central role of Mic10 in the mitochondrial contact site and cristae organizing system. Cell Metabol. *21*, 747–755. https://doi.org/10.1016/j.cmet.2015.04.007.
12. Hessenberger, M., Zerbes, R.M., Rampelt, H., Kunz, S., Xavier, A.H., Purfürst, B., Lilie, H., Pfanner, N., van der Laan, M., and Daumke, O. (2017). Regulated membrane remodeling by Mic60 controls formation of mitochondrial crista junctions. Nat. Commun. *8*, 15258. https://doi.org/10.1038/ncomms15258.
13. Bock-Bierbaum, T., Funck, K., Wollweber, F., Lisicki, E., von der Malsburg, K., von der Malsburg, A., Laborenz, J., Noel, J.K., Hessenberger, M., Jungbluth, S., et al. (2022). Structural insights into crista junction formation by the Mic60-Mic19 complex. Sci. Adv. *8*, eabo4946. https://doi.org/10.1126/sciadv.abo4946.
14. Tarasenko, D., Barbot, M., Jans, D.C., Kroppen, B., Sadowski, B., Heim, G., Möbius, W., Jakobs, S., and Meinecke, M. (2017). The MICOS component Mic60 displays a conserved membrane-bending activity that is necessary for normal cristae morphology. J. Cell Biol. *216*, 889–899. https://doi.org/10.1083/jcb.201609046.
15. Anand, R., Strecker, V., Urbach, J., Wittig, I., and Reichert, A.S. (2016). Mic13 Is Essential for Formation of Crista Junctions in Mammalian Cells. PLoS One *11*, e0160258. https://doi.org/10.1371/journal.pone.0160258.
16. Guarani, V., McNeill, E.M., Paulo, J.A., Huttlin, E.L., Fröhlich, F., Gygi, S.P., Van Vactor, D., and Harper, J.W. (2015). QIL1 is a novel mitochondrial protein required for MICOS complex stability and cristae morphology. Elife *4*, e06265. https://doi.org/10.7554/eLife.06265.

17. Urbach, J., Kondadi, A.K., David, C., Naha, R., Deinert, K., Reichert, A.S., and Anand, R. (2021). Conserved GxxxG and WN motifs of MIC13 are essential for bridging two MICOS subcomplexes. Biochim. Biophys. Acta Biomembr. *1863*, 183683. https://doi.org/10.1016/j.bbamem.2021.183683.

18. Zerbes, R.M., van der Klei, I.J., Veenhuis, M., Pfanner, N., van der Laan, M., and Bohnert, M. (2012). Mitofilin complexes: conserved organizers of mitochondrial membrane architecture. Biol. Chem. *393*, 1247–1261. https://doi.org/10.1515/hsz-2012-0239.

19. An, J., Shi, J., He, Q., Lui, K., Liu, Y., Huang, Y., and Sheikh, M.S. (2012). CHCM1/CHCHD6, novel mitochondrial protein linked to regulation of mitofilin and mitochondrial cristae morphology. J. Biol. Chem. *287*, 7411–7426. https://doi.org/10.1074/jbc.M111.277103.

20. Sakowska, P., Jans, D.C., Mohanraj, K., Riedel, D., Jakobs, S., and Chacinska, A. (2015). The Oxidation Status of Mic19 Regulates MICOS Assembly. Mol. Cell Biol. *35*, 4222–4237. https://doi.org/10.1128/MCB.00578-15.

21. Anand, R., Kondadi, A.K., Meisterknecht, J., Golombek, M., Nortmann, O., Riedel, J., Peifer-Weiß, L., Brocke-Ahmadinejad, N., Schlütermann, D., Stork, B., et al. (2020). MIC26 and MIC27 cooperate to regulate cardiolipin levels and the landscape of OXPHOS complexes. Life Sci. Alliance *3*, e202000711. https://doi.org/10.26508/lsa.202000711.

22. Tang, J., Zhang, K., Dong, J., Yan, C., Hu, C., Ji, H., Chen, L., Chen, S., Zhao, H., and Song, Z. (2020). Sam50-Mic19-Mic60 axis determines mitochondrial cristae architecture by mediating mitochondrial outer and inner membrane contact. Cell Death Differ. *27*, 146–160. https://doi.org/10.1038/s41418-019-0345-2.

23. Huynen, M.A., Mühlmeister, M., Gotthardt, K., Guerrero-Castillo, S., and Brandt, U. (2016). Evolution and structural organization of the mitochondrial contact site (MICOS) complex and the mitochondrial intermembrane space bridging (MIB) complex. Biochim. Biophys. Acta *1863*, 91–101. https://doi.org/10.1016/j.bbamcr.2015.10.009.

24. Xie, J., Marusich, M.F., Souda, P., Whitelegge, J., and Capaldi, R.A. (2007). The mitochondrial inner membrane protein mitofilin exists as a complex with SAM50, metaxins 1 and 2, coiled-coil-helix coiled-coil-helix domain-containing protein 3 and 6 and DnaJC11. FEBS Lett. *581*, 3545–3549. https://doi.org/10.1016/j.febslet.2007.06.052.

25. Guarani, V., Jardel, C., Chretien, D., Lombes, A., Benit, P., Labasse, C., Lacene, E., Bourillon, A., Imbard, A., Benoist, J.F., et al. (2016). QIL1 mutation causes MICOS disassembly and early onset fatal mitochondrial encephalopathy with liver disease. Elife *5*, 17163. https://doi.org/10.7554/eLife.17163.

26. Russell, B.E., Whaley, K.G., Bove, K.E., Labilloy, A., Lombardo, R.C., Hopkin, R.J., Leslie, N.D., Prada, C., Assouline, Z., Barcia, G., et al. (2019). Expanding and Underscoring the Hepato-Encephalopathic Phenotype of QIL1/MIC13. Hepatology *70*, 1066–1070. https://doi.org/10.1002/hep.30627.

27. Zeharia, A., Friedman, J.R., Tobar, A., Saada, A., Konen, O., Fellig, Y., Shaag, A., Nunnari, J., and Elpeleg, O. (2016). Mitochondrial hepato-encephalopathy due to deficiency of QIL1/MIC13 (C19orf70), a MICOS complex subunit. Eur. J. Hum. Genet. *24*, 1778–1782. https://doi.org/10.1038/ejhg.2016.83.

28. Godiker, J., Gruneberg, M., DuChesne, I., Reunert, J., Rust, S., Westermann, C., Wada, Y., Classen, G., Langhans, C.D., Schlingmann, K.P., et al. (2018). QIL1-dependent assembly of MICOS complex-lethal mutation in C19ORF70 resulting in liver disease and severe neurological retardation. J. Hum. Genet. *63*, 707–716. https://doi.org/10.1038/s10038-018-0442-y.

29. Marco-Hernández, A.V., Tomás-Vila, M., Montoya-Filardi, A., Barranco-González, H., Vilchez Padilla, J.J., Azorín, I., Smeyers Dura, P., Monfort-Membrado, S., Pitarch-Castellano, I., and Martínez-Castellano, F. (2021). Mitochondrial developmental encephalopathy with bilateral optic neuropathy related to homozygous variants in IMMT gene. Clin Genet *101*, 233–241. https://doi.org/10.1111/cge.14093.

30. Tsai, P.I., Lin, C.H., Hsieh, C.H., Papakyrikos, A.M., Kim, M.J., Napolioni, V., Schoor, C., Couthouis, J., Wu, R.M., Wszolek, Z.K., et al. (2018). PINK1 Phosphorylates MIC60/Mitofilin to Control Structural Plasticity of Mitochondrial Crista Junctions. Mol. Cell *69*, 744–756. https://doi.org/10.1016/j.molcel.2018.01.026.

31. Peifer-Weiß, L., Kurban, M., David, C., Lubeck, M., Kondadi, A.K., Nemer, G., Reichert, A.S., and Anand, R. (2023). An X-linked nonsense APOO/MIC26 variant causes a lethal mitochondrial disease with progeria-like phenotypes. Clin Genet *104*, 659–668. https://doi.org/10.1111/cge.14420.

32. Christie, D.A., Lemke, C.D., Elias, I.M., Chau, L.A., Kirchhof, M.G., Li, B., Ball, E.H., Dunn, S.D., Hatch, G.M., and Madrenas, J. (2011). Stomatin-like protein 2 binds cardiolipin and regulates mitochondrial biogenesis and function. Mol. Cell Biol. *31*, 3845–3856. https://doi.org/10.1128/MCB.05393-11.

33. Tondera, D., Grandemange, S., Jourdain, A., Karbowski, M., Mattenberger, Y., Herzig, S., Da Cruz, S., Clerc, P., Raschke, I., Merkwirth, C., et al. (2009). SLP-2 is required for stress-induced mitochondrial hyperfusion. EMBO J. *28*, 1589–1600. https://doi.org/10.1038/emboj.2009.89.

34. Wai, T., Saita, S., Nolte, H., Müller, S., König, T., Richter-Dennerlein, R., Sprenger, H.G., Madrenas, J., Mühlmeister, M., Brandt, U., et al. (2016). The membrane scaffold SLP2 anchors a proteolytic hub in mitochondria containing PARL and the i-AAA protease YME1L. EMBO Rep. *17*, 1844–1856. https://doi.org/10.15252/embr.201642698.

35. Koob, S., Barrera, M., Anand, R., and Reichert, A.S. (2015). The non-glycosylated isoform of MIC26 is a constituent of the mammalian MICOS complex and promotes formation of crista junctions. Biochim. Biophys. Acta *1853*, 1551–1563. https://doi.org/10.1016/j.bbamcr.2015.03.004.

36. Rampelt, H., Wollweber, F., Gerke, C., de Boer, R., van der Klei, I.J., Bohnert, M., Pfanner, N., and van der Laan, M. (2018). Assembly of the Mitochondrial Cristae Organizer Mic10 Is Regulated by Mic26-Mic27 Antagonism and Cardiolipin. J. Mol. Biol. *430*, 1883–1890. https://doi.org/10.1016/j.jmb.2018.04.037.

37. Li, H., Ruan, Y., Zhang, K., Jian, F., Hu, C., Miao, L., Gong, L., Sun, L., Zhang, X., Chen, S., et al. (2016). Mic60/Mitofilin determines MICOS assembly essential for mitochondrial dynamics and mtDNA nucleoid organization. Cell Death Differ. *23*, 380–392. https://doi.org/10.1038/cdd.2015.102.

38. Jans, D.C., Wurm, C.A., Riedel, D., Wenzel, D., Stagge, F., Deckers, M., Rehling, P., and Jakobs, S. (2013). STED super-resolution microscopy reveals an array of MINOS clusters along human mitochondria. Proc. Natl. Acad. Sci. USA *110*, 8936–8941. https://doi.org/10.1073/pnas.1301820110.

39. Stoldt, S., Stephan, T., Jans, D.C., Brüser, C., Lange, F., Keller-Findeisen, J., Riedel, D., Hell, S.W., and Jakobs, S. (2019). Mic60 exhibits a coordinated clustered distribution along and across yeast and mammalian mitochondria. Proc. Natl. Acad. Sci. USA *116*, 9853–9858. https://doi.org/10.1073/pnas.1820364116.

40. Ott, C., Dorsch, E., Fraunholz, M., Straub, S., and Kozjak-Pavlovic, V. (2015). Detailed analysis of the human mitochondrial contact site complex indicate a hierarchy of subunits. PLoS One *10*, e0120213. https://doi.org/10.1371/journal.pone.0120213.

41. Beninca, C., Zanette, V., Brischigliaro, M., Johnson, M., Reyes, A., Valle, D.A.D., A, J.R., Degiorgi, A., Yeates, A., Telles, B.A., et al. (2021). Mutation in the MICOS subunit gene APOO (MIC26) associated with an X-linked recessive mitochondrial myopathy, lactic acidosis, cognitive impairment and autistic features. J. Med. Genet. *58*, 155–167. https://doi.org/10.1136/jmedgenet-2020-106861.

42. van der Laan, M., Horvath, S.E., and Pfanner, N. (2016). Mitochondrial contact site and cristae organizing system. Curr. Opin. Cell Biol. *41*, 33–42. https://doi.org/10.1016/j.ceb.2016.03.013.

43. Zerbes, R.M., Höß, P., Pfanner, N., van der Laan, M., and Bohnert, M. (2016). Distinct Roles of Mic12 and Mic27 in the Mitochondrial Contact

Site and Cristae Organizing System. J. Mol. Biol. *428*, 1485–1492. https://doi.org/10.1016/j.jmb.2016.02.031.

44. Viana, M.P., Levytskyy, R.M., Anand, R., Reichert, A.S., and Khalimonchuk, O. (2021). Protease OMA1 modulates mitochondrial bioenergetics and ultrastructure through dynamic association with MICOS complex. iScience *24*, 102119. https://doi.org/10.1016/j.isci.2021.102119.

45. Kondadi, A.K., Anand, R., and Reichert, A.S. (2020). Cristae Membrane Dynamics - A Paradigm Change. Trends Cell Biol. *30*, 923–936. https://doi.org/10.1016/j.tcb.2020.08.008.

46. Morita, S., Kojima, T., and Kitamura, T. (2000). Plat-E: an efficient and stable system for transient packaging of retroviruses. Gene Ther. *7*, 1063–1066. https://doi.org/10.1038/sj.gt.3301206.

47. Chiu, J., Tillett, D., Dawes, I.W., and March, P.E. (2008). Site-directed, Ligase-Independent Mutagenesis (SLIM) for highly efficient mutagenesis of plasmids greater than 8kb. J. Microbiol. Methods *73*, 195–198. https://doi.org/10.1016/j.mimet.2008.02.013.

48. Kulak, N.A., Pichler, G., Paron, I., Nagaraj, N., and Mann, M. (2014). Minimal, encapsulated proteomic-sample processing applied to copy-number estimation in eukaryotic cells. Nat. Methods *11*, 319–324. https://doi.org/10.1038/nmeth.2834.

49. Schindelin, J., Arganda-Carreras, I., Frise, E., Kaynig, V., Longair, M., Pietzsch, T., Preibisch, S., Rueden, C., Saalfeld, S., Schmid, B., et al. (2012). Fiji: an open-source platform for biological-image analysis. Nat. Methods *9*, 676–682. https://doi.org/10.1038/nmeth.2019.

50. Tyanova, S., Temu, T., Sinitcyn, P., Carlson, A., Hein, M.Y., Geiger, T., Mann, M., and Cox, J. (2016). The Perseus computational platform for comprehensive analysis of (prote)omics data. Nat. Methods *13*, 731–740. https://doi.org/10.1038/nmeth.3901.

51. Barrera, M., Koob, S., Dikov, D., Vogel, F., and Reichert, A.S. (2016). OPA1 functionally interacts with MIC60 but is dispensable for crista junction formation. FEBS Lett. *590*, 3309–3322. https://doi.org/10.1002/1873-3468.12384.

52. Olsen, J.V., de Godoy, L.M., Li, G., Macek, B., Mortensen, P., Pesch, R., Makarov, A., Lange, O., Horning, S., and Mann, M. (2005). Parts per Million Mass Accuracy on an Orbitrap Mass Spectrometer via Lock Mass Injection into a C-trap. Mol. Cell. Proteomics *4*, 2010–2021. https://doi.org/10.1074/mcp.T500030-MCP200.

53. Cox, J., and Mann, M. (2008). MaxQuant enables high peptide identification rates, individualized p.p.b.-range mass accuracies and proteome-wide protein quantification. Nat. Biotechnol. *26*, 1367–1372. https://doi.org/10.1038/nbt.1511.

STAR★METHODS

KEY RESOURCES TABLE

REAGENT or RESOURCE	SOURCE	IDENTIFIER
Antibodies		
MIC13 peptide (CKAREYSKEGWEYVKARTK)	Pineda	Custom-made (Anand et al.[15])
MIC19	Proteintech	Cat# 25625-1-AP; RRID: AB_2687533
MIC25	Proteintech	Cat# 20639-1-AP; RRID: AB_1069767
MIC60 peptide (CTDHPEIGEGKPTPALSEEAS)	Pineda	Custom-made (Barrera et al.[47])
MIC26	Thermo Fisher Scientific	Cat# MA5-15493; RRID: AB_10982238
MIC27	Sigma-Aldrich	Cat# HPA000612; RRID: AB_1078594
MIC60	Abcam	Cat# ab110329; RRID: AB_10859613
SLP2 (rabbit)	Abcam	Cat# ab102051; RRID: AB_10863523
SLP2 (mouse)	OriGene	Cat# TA808240; RRID: AB_2628756
beta-tubulin	Cell Signaling Technology	Cat# 4466; RRID: AB_1904176
HSP60	Sigma	Cat# SAB4501464; RRID: AB_10746162
Mt-CO2	Abcam	Cat# ab110258; RRID: AB_10887758
YME1L	Proteintech	Cat# 11510-1-AP; RRID: AB_2217459
MTX1	Abcam	Cat# ab233205; RRID: AB_3665905
Goat anti-mouse IgG HRP-conjugated antibody	Abcam	Cat# ab97023; RRID: AB_10679675
goat anti-rabbit IgG HRP-conjugated antibody	Dianova	Cat# 111-035-144; RRID: AB_2307391
635P goat-*anti*-rabbit	Aberrior STAR	Cat# ST635P-1002-500UG; RRID: AB_2893229
Bacterial and virus strains		
DH5α competent cells	Thermo Fisher Scientific	18265017
Chemicals, peptides, and recombinant proteins		
Glutaraldehyde	Serva	23114.02
Sodium cacodylate	Serva	15540
Osmium tetroxide	Science Services	E19110
Uranyl Acetate	Merck	8473
Phosphotungstic acid hydrate	Merck	1.00582.0100
D.E.R.® 736	Serva	18247.01
ERL-4221D, Epoxycyclohexylmethyl-3,4-epoxycyclohexylcarboxylate	Serva	21041.02
Nonerylsuccinic Anhydride Pure	Serva	30812.01
Dimethylaminomethanol	Serva	20130
Stable glutamine	PAN-Biotech	P04-82100
PenStrep	Sigma-Aldrich	P4333-100mL
Sodium pyruvate	Gibco	11360070
Paraformaldehyde	Sigma-Aldrich	P6148
Triton X-100	Sigma-Aldrich	T8787-100ML
Digitonin	Serva	19550.02
Mannitol	Roth	4175.1
Saccharose	Merck	1.07653
EDTA	Merck	1.08418.1000
HEPES	Sigma Aldrich	H4034-500G
TRIS	Roth	AE15.3
Protease Inhibitor tablets	Roche	5056489001
Trehalose	Sigma Aldrich	T0331

(*Continued on next page*)

Continued

REAGENT or RESOURCE	SOURCE	IDENTIFIER
NaCl	Roth	9265.2
KCl	Merck	7447-40-7
BSA	Roth	0052–3
Aminohexanoic acid	Sigma Aldrich	A2504-500G
Imidazole	Sigma Aldrich	I5513-25G
Coomassie Brilliant Blue G-250 Dye	Thermo Fisher Scientific	20279
Critical commercial assays		
Duolink® *In Situ* Red Starter Kit Mouse/Rabbit	Sigma-Aldrich	DUO92101-1KT
Gibson assembly cloning Kit	NEB	E2611L
MYC trap agarose beads	ChromoTek	yta-100
AntiFLAG m2 affinity beads	Sigma-Aldrich	A2220-5ML
Protein A Sepharose beads	Invitrogen	101041
Novagen GeneJuice Transfection Reagent	Merck	70967–6
Lipofectamine RNAiMAX	Invitrogen	13778–075
Deposited data		
Mass spectrometry proteomics data for MIC13 interactome	PRIDE	PRIDE: PXD044968
Experimental models: Cell lines		
Human: Flp-In T-REx HEK293	Thermo Fisher Scientific	Cat# R78007; RRID: CVCL_U427
Human: HeLa	ATCC	Cat# HeLa CCL-2 ™; RRID: CVCL_0030
Human: 293FT Cell Line	Thermo Fisher Scientific	R70007
Human: Plat-E cells	Morita et al.[48]	N/A
Flp-In T-REx HEK293 MIC13 knockout (*MIC13* KO)	Anand et al.[15]	N/A
Flp-In T-REx HEK293 SLP2 knockout (*SLP2* KO)	This study	N/A
Flp-In T-REx HEK293 MIC26 knockout (*MIC26* KO)	This study	N/A
Flp-In T-REx HEK293 MIC27 knockout (*MIC27* KO)	This study	N/A
Flp-In T-REx HEK293 MIC10 knockout (*MIC10* KO)	This study	N/A
Flp-In T-REx HEK293 MIC60 knockout (*MIC60* KO)	This study	N/A
Flp-In T-REx HEK293 MIC25 knockout (*MIC25* KO)	This study	N/A
Flp-In T-REx HEK293 MIC19 knockout (*MIC19* KO)	This study	
Flp-In T-REx HEK293 MIC13-SLP2 double knockout (*MIC13-SLP2* DKO)	This study	N/A
Flp-In T-REx HEK293 WT stably expressing SLP2-MYC	This study	N/A
Flp-In T-REx HEK293 *MIC10* KO stably expressing SLP2-MYC	This study	N/A
Flp-In T-REx HEK293 *MIC13* KO stably expressing SLP2-MYC	This study	N/A
Flp-In T-REx HEK293 *MIC26* KO stably expressing SLP2-MYC	This study	N/A
Flp-In T-REx HEK293 *MIC27* KO stably expressing SLP2-MYC	This study	N/A
Flp-In T-REx HEK293 *MIC60* KO stably expressing SLP2-MYC	This study	N/A
Flp-In T-REx HEK293 *MIC19* KO stably expressing SLP2-MYC	This study	N/A
Flp-In T-REx HEK293 *MIC25* KO stably expressing SLP2-MYC	This study	N/A
Flp-In T-REx HEK293 *MIC13-SLP2* DKO stably expressing SLP2-MYC	This study	N/A
Flp-In T-REx HEK293 *SLP2* KO stably expressing SLP2-MYC	This study	N/A
Flp-In T-REx HEK293 *SLP2* KO stably expressing pMSCV-puro (empty vector control)	This study	N/A
Flp-In T-REx HEK293 MIC13 knockout (MIC13 KO) stably expressing MIC13-FLAG	Urbach et al.[17]	N/A
Flp-In T-REx HEK293 MIC13 knockout (*MIC13* KO) stably expressing pMSVC-puro (empty vector control)	Urbach et al.[17]	N/A
Flp-In T-REx HEK293 *MIC13-SLP2* KO stably expressing MIC13-FLAG	This study	N/A

(*Continued on next page*)

Continued

REAGENT or RESOURCE	SOURCE	IDENTIFIER
Flp-In T-REx HEK293 WT stably expressing pLIX403	This study	N/A
Flp-In T-REx HEK293 *MIC13* KO stably expressing pLIX403-MIC13-FLAG	This study	N/A
Flp-In T-REx HEK293 *MIC13-SLP2* DKO stably expressing pLIX403-MIC13-FLAG	This study	N/A
Flp-In T-REx HEK293 WT stably expressing GIPZ Non-Silencing shRNA	This study	N/A
Flp-In T-REx HEK293 *MIC13* KO stably expressing GIPZ Non-Silencing shRNA	This study	N/A
Flp-In T-REx HEK293 *SLP2* KO stably expressing GIPZ Non-Silencing shRNA	This study	N/A
Flp-In T-REx HEK293 *MIC13-SLP2* DKO stably expressing GIPZ Non-Silencing shRNA	This study	N/A
Flp-In T-REx HEK293 WT stably expressing YME1L-shRNA	This study	N/A
Flp-In T-REx HEK293 *MIC13* KO stably expressing YME1L-shRNA	This study	N/A
Flp-In T-REx HEK293 *SLP2* KO stably expressing YME1L-shRNA	This study	N/A
Flp-In T-REx HEK293 *MIC13-SLP2* DKO stably expressing YME1L-shRNA	This study	N/A
Oligonucleotides		
SLP2HA_FP_Plasmid	Sigma	TAACGAATTCTACCGGGTAGGG
SLP2HA_RP_Plasmid	Sigma	ACCTCGAGAGATCTAATTCCGG
SLP2HA_FP_Insert	Sigma	AATTAGATCTCTCGAGGTAAGCTTGGTACC ATGCTGGCG
SLP2HA_RP_Insert	Sigma	ACCCGGTAGAATTCGTTAGGCCGCTCTAGA CTCGAGTTTAG
SLP2_MYC_FPS3	Sigma	TAACGAATTCTACCGGGTAGGGGAGGCGC
SLP2_MYC_RPS3	Sigma	AGAGCCTCCACCCCCACTCATCTTGACTCG
SLP2_MYC_FPL3	Sigma	GAACAAAAACTCATCTCAGAAGAGGATCTGT AACGAATTCTACCGGGTAGGGGAGGCGC
SLP2_MYC_RPL3	Sigma	CAGATCCTCTTCTGAGATGAGTTTTTGTTCA GAGCCTCCACCCCCACTCATCTTGACTCG
FP_Tet_pLIX_VECTOR	Integrated DNA Technology	CTTTCTTGTACAAAGTGG
RP_Tet_pLIX_VECTOR	Integrated DNA Technology	GCTTTTTTGTACAAACTT
FP_Tet_MIC13_Insert	Integrated DNA Technology	AAGTTTGTACAAAAAAGCCTCTCGAGGTAT GGTGGCC
RP_Tet_MIC13_Insert	Integrated DNA Technology	CCACTTTGTACAAGAAAGGAATTCGTTATTT GTCATCGTCATC
OMA1 siRNA	Thermo Fisher Scientific	AM16704; Sense: GGAAAUUUGGAGGAUUA CCtt AntiSense: GGUAAUCCUCCAAAUUUCCtt
Recombinant DNA		
Human SLP2-HA ORF	Sino Biologicals	HG16147-CY
pMSCV puro MIC13-FLAG	Urbach et al.[17]	N/A
pMSCV puro SLP2-MYC	This study	N/A
pMSCV puro SLP2-HA	This study	N/A
pGIPZ-non-silencing-Control-shRNA	Horizon Discovery	RHS4346
pGIPZ-YME1L-shRNA	Horizon Discovery	RHS4430-200157017, RHS4430-200215861, RHS4430-200221198, RHS4430-200268420, RHS4430-200273633, RHS4430-200280144

(*Continued on next page*)

Continued

REAGENT or RESOURCE	SOURCE	IDENTIFIER
pLIX403	Addgene	41395
pLIX403 MIC13-FLAG	This study	N/A
CRISPR-Cas9 double nickase plasmid: SLP2	Santa Cruz Biotechnology	sc-403638-NIC
CRISPR-Cas9 double nickase plasmid: MIC10	Santa Cruz Biotechnology	sc-417564-NIC
CRISPR-Cas9 double nickase plasmid: MIC19	Santa Cruz Biotechnology	sc-408682-NIC
CRISPR-Cas9 double nickase plasmid: MIC25	Santa Cruz Biotechnology	sc-413621-NIC
CRISPR-Cas9 double nickase plasmid: MIC26	Santa Cruz Biotechnology	sc-413137-NIC
CRISPR-Cas9 double nickase plasmid: MIC27	Santa Cruz Biotechnology	sc-414464-NIC
CRISPR-Cas9 double nickase plasmid: MIC60	Santa Cruz Biotechnology	sc-403617-NIC
psPAX2	Addgene	12260
pMD2.G	Addgene	12259
Software and algorithms		
GraphPad Prism	www.graphpad.com	Version 10
CorelDRAW Graphics Suite 2017	Corel Corporation	Version 19
Microsoft Excel 2019	Microsoft Office Professional Plus 2019	N/A
Fiji	Schindelin et al.[49]	N/A
Volocity	PerkinElmer	Version 6.3.0
FUSION software	Vilber	N/A
MaxQuant	Cox and Mann[50]	1.6.1.0
Perseus	Tyanova et al.[51]	1.5.6.0
Other		
DMEM 1 g/L glucose	PAN-Biotech	Cat# P04-01500
DMEM 4.5 g/L glucose	PAN-Biotech	Cat# P04-82100
FBS	Capricorn Scientific	Cat# FBS-11A
Milk powder	Roth	T145.4
Goat serum	Sigma-Aldrich	S26-M

EXPERIMENTAL MODEL AND STUDY PARTICIPANT DETAILS

Cell lines and cell culture

Flp-In T-REx HEK293 Cell Line (Thermofisher scientific, catalog number R78007) (RRID:CVCL_U427) (Female) and HeLa cells (HeLa CCL-2 ATCC) (RRID:CVCL_0030) (Female) were cultured in Dulbecco's modified Eagle medium (DMEM) with 1 g/L glucose and sodium pyruvate (PAN-Biotech, P04-01500) supplemented with 1% stable glutamine (P04-82100), 1% penicillin-streptomycin (Sigma-Aldrich, P4333-100mL), 10% fetal bovine serum (FBS) (Capricorn Scientific, FBS-11A). Plat-E[48] and HEK293FT cells were cultured in DMEM high glucose medium (PAN-Biotech, P04-03500) supplemented with 10% FBS, 1% stable glutamine, 1% sodium pyruvate (Gibco, 11360070). GIPZ-Control- Flp-In T-REx HEK293 and GIPZ-YME1LshRNA- Flp-In T-REx HEK293 cells were cultured in DMEM 1 g/L glucose medium containing sodium pyruvate supplemented with 1% stable glutamine, 10% FBS, 1% penicillin-streptomycin and 1% Non-Essential Amino Acids Solution (NEAA) (PAN-Biotech, P08-32100). All cells were cultured at 37°C with 5% CO_2. All cell lines generated are listed in Key resources table.

METHOD DETAILS

Co-immunoprecipitation coupled mass spectrometry

Co-IP was performed with Protein A Sepharose CL-4B beads (Invitrogen, 101041) and affinity purified MIC13 antibody was linked to the beads. Isolated mitochondria from Flp-In T-REx HEK293 WT or *MIC13* KO were solubilized with isotonic buffer (150 mM NaCl, 10 mM Tris/HCl (pH 7.5), 5 mM EDTA, 1x protease inhibitor cocktail) supplemented with 5 μL of 10% Digitonin (2 g/g of protein) and added to the beads with subsequent incubation in 4°C under rotation conditions. Beads were washed several times, transferred into a new tube in 10mM Tris, pH 7.4. Beads were resuspended in 50 μL 6M GdmCl, 50 mM Tris/HCl, pH 8.5 and incubated at 95°C for 5 min. Sample were diluted with 25 mM Tris/HCl, pH 8.5, 10% acetonitrile to obtain a final GdmCl concentration of 0.6 M. Proteins were digested with 1 μg Trypsin (sequencing grade, Promega) overnight at 37°C under gentle agitation. Digestion was stopped by

adding trifluoroacetic acid to a final concentration of 0.5%. Peptides were loaded on multi-stop-and-go tip (StageTip) containing six C18 discs. Purification and elution of peptides was performed as described in Kulak et al.[52] Peptides were eluted in wells of microtiter plates and peptides were dried and resolved in 1% acetonitrile, 0.1% formic acid. Liquid chromatography/mass spectrometry (LC/MS) was performed on Thermo Scientific Q Exactive Plus equipped with an ultra-high performance liquid chromatography unit (Thermo Scientific Dionex Ultimate 3000) and a Nanospray Flex Ion-Source (Thermo Scientific). Peptides were loaded on a C18 reversed-phase precolumn (Thermo Scientific) followed by separation on a with 2.4 μm Reprosil C18 resin (Dr. Maisch GmbH) in-house packed picotip emitter tip (diameter 100 μm, 30 cm long from New Objectives) using an gradient from mobile phase A (4% acetonitrile, 0.1% formic acid) to 60% mobile phase B (99% acetonitrile, 0.1% formic acid) for 90 min with a flow rate 350 nL/min. MS data were recorded by data dependent acquisition Top10 method selecting the most abundant precursor ions in positive mode for HCD fragmentation. Lock mass option[53] was enabled to ensure high mass accuracy between multiple runs. The Full MS scan range was 300–2000 m/z with resolution of 70000, and an automatic gain control (AGC) value of 3*106 total ion counts with a maxim al ion injection time of 160 ms. Only higher charged ions (2+) were selected for MS/MS scans with a resolution of 17500, an isolation window of 2 m/z and an automatic gain control value set to 105 ions with a maximal ion injection time of 150 ms. Selected ions were excluded in a time frame of 30s following fragmentation event. Fullscan data were acquired in profile and fragments in centroid mode by Xcalibur software. For data analysis MaxQuant 1.6.1.0 (Cox and Mann, 2008, Nat. Biotechnology),[50] Perseus 1.5.6.0 (Tyranova et al. 2016)[51] and Excel (Microsoft Office 2013) were used. N-terminal acetylation (+42.01) and oxidation of methionine (+15.99) were selected as variable modifications and carbamidomethylation (+57.02) on cysteines as a fixed modification. The human reference proteome set (Uniprot, July 2017, 701567 entries) was used to identify peptides and proteins with a false discovery rate (FDR) less than 1%. Minimal ratio count for label-free quantification (LFQ) was 1. Reverse identifications and common contaminants were removed and the dataset was reduced to proteins that were identified in at least 5 of 7 samples in one experimental group. Missing LFQ or IBAQ values were replaced by random background values. Significant interacting proteins were determined by permutation-based false discovery rate (FDR) calculation and students T-Test. The mass spectrometry proteomics data have been deposited to the ProteomeXchange Consortium via the PRIDE partner repository with the dataset identifier PRIDE: PXD044968.

Proximity ligation assay

PLA was carried out with Duolink *In Situ* Red Starter Kit Mouse/Rabbit (Sigma-Aldrich, DUO92101-1KT) following manufacturer's protocol with minor modifications. Briefly, HeLa cells were fixed using 4% paraformaldehyde (Sigma-Aldrich, P6148) for 20 min in room temperature and washed with PBS 3x with subsequent permeabilization with 0.15% Triton X-100 (Sigma-Aldrich, T8787-100ML) at room temperature for 15 min followed by PBS wash. Permeabilized cells were blocked with blocking solution (provided in kit) for 1 h in 37°C. Blocking solution was removed and primary antibodies with 1:100 dilution ratio was added to the samples and incubation was carried out at 37°C for 2 h. The following primary antibodies were used: MIC10 (Abcam, 84969), MIC13 (custom made by Pineda (Berlin) against human MIC13 peptide CKAREYSKEGWEYVKARTK), MIC19 (Proteintech, 25625-1-AP), MIC25 (Proteintech, 20639-1-AP), MIC26 (Thermofisher Scientific, MA5-15493), MIC27 (Sigma-Aldrich, HPA000612-100UL), MIC60 (Abcam, ab110329), SLP2 (Abcam, ab102051), SLP2 (OriGene, TA808240), Mt-CO2 (Abcam, ab110258)), OPA1 (custom-made, Pineda against human OPA1 using peptide CDLKKVREIQEKLDAFIEALHQEK,[47] Vinculin (Sigma-Aldrich, V9131). Subsequent ligation of PLA probes and amplification of circular DNA probes was carried out following manufacturer's protocol. PLA signals were visualized in PerkinElmer spinning disc confocal microscope equipped with a 60× oil objective.

CRISPR-Cas9 knockout generation

CRISPR-Cas9 double nickase plasmid (Santa Cruz Biotechnology, SLP2: sc-403638-NIC, MIC26: sc-413137-NIC, MIC60: sc-403617-NIC, MIC25: sc-413621-NIC, MIC19: sc-408682-NIC, MIC10: sc-417564-NIC, MIC27: sc-414464-NIC) was transfected with GeneJuice (Sigma-Aldrich, 70967-3) in Flp-In T-REx HEK293 WT, *MIC13* KO parental lines to generate KO and double KO cell lines. Briefly, cell lines were transfected at 60–70% confluency with 1 μg of double nickase plasmid and incubated for 48 h followed by 2.5 μg/mL puromycin selection for 24 h with subsequent single cell sorting based on green fluorescent protein (GFP) expression using flow cytometry in 96 well plate. Cells were incubated and upon visible colonies, cells were sub-cultured and KO screen was performed with western blotting. Cell lines showing no immune reactivity to respective antibodies were termed as KOs or double KOs.

Molecular cloning

Human SLP2-HA ORF (Sino Biologicals, HG16147-CY) was cloned into pMSCVpuro vector using Gibson assembly cloning kit (NEB, E2611L), following manufacturer's protocol. HA tag was replaced with MYC tag with Site Directed and Ligation Independent Mutagenesis (SLIM)[49] to generate pMSCV-SLP2-MYC. Human MIC13-Flag from pMSCV puro MIC13-FLAG[17] was cloned into pLIX403 (Addgene, 41395) with Gibson assembly following manufacturers protocol. Primer sequences for Gibson assembly and SLIM are provided in key resources table.

Generation of stable cell lines and siRNA knockdown

For retroviral transduction, Plat-E cells[21] were transfected with 1 μg of pMSCV-MIC13Flag or pMSCV-SLP2MYC and 1 μg of pVSV-G with 3.5 μL of GeneJuice per wells of 6-well plate. After 72 h incubation, viral supernatant was added to the target cells. Media was

replaced with puromycin containing media (2.5 μg/mL) 48 h of transduction. Puromycin selection was carried out for 2 weeks and successful expression of exogenous protein was validated with western blot. For lentiviral transduction, HEK293FT cells were transfected with 1ug of pLIX403 EV or pLIX403-MIC13-Flag or pGIPZ-non-silencing-Control-shRNA (Horizon Discovery, RHS4346) or pGIPZ-YME1L-shRNA (Horizon Discovery, RHS4430-200157017, RHS4430-200215861, RHS4430-200221198, RHS4430-200268420, RHS4430-200273633, RHS4430-200280144) along with 1μg of psPAX2 (Addgene, 12260) and pMD2.G (Addgene, 12259) was transfected using GeneJuice. 72 h post transfection, viral supernatant was collected and added on target cell lines. Media was replaced with puromycin (2.5 μg/mL) containing media and selection was carried out for about 2 weeks. Successful exogenous protein expression or knockdown was confirmed with western blotting.

OMA1 siRNA (Thermo fisher scientific, AM16704 with the following sequence Sense: GGAAAUUUGGAGGAUUACCtt AntiSense: GGUAAUCCUCCAAAUUUCCtt) was transfected to the cells using Lipofectamine RNAiMAX (Thermo fisher scientific).

SDS PAGE and western blot

Cells were grown in 6-well dishes and harvested with cold PBS upon 70–90% confluency followed by protein extraction by RIPA lysis. Protein concentration was determined by Lowry method (Bio-Rad, 5000113, 5000114, 5000115) and samples were prepared using Laemmli loading buffer. Proteins were separated using 10% or 15% SDS-PAGE with subsequent transfer on nitrocellulose membrane (Amersham, 10600004) followed by 1 h of blocking using 5% skimmed milk (Carlroth, 68514-61-4). Membranes were incubated overnight in 4°C under shaking conditions in primary antibodies: MIC10 (Abcam, 84969), MIC13 (custom made by Pineda (Berlin) against human MIC13 peptide CKAREYSKEGWEYVKARTK),[15] MIC19 (Proteintech, 25625-1-AP), MIC25 (Proteintech, 20639-1-AP), MIC26 (Thermo fisher Scientific, MA5-15493), MIC27 (Sigma-Aldrich, HPA000612-100UL), MIC60 (Abcam, ab110329), SLP2 (Abcam, ab102051), beta-tubulin (Cell Signaling Technology, 2128S), HSP60 (sigma, SAB4501464), Mt-CO2 (Abcam, ab110258), YME1L (Proteintech, 11510-1-AP), MTX1 (Abcam, ab233205). Following primary antibody incubation, membranes were washed in TBST and probed with Goat anti-mouse IgG HRP-conjugated antibody (Abcam, ab97023) or goat anti-rabbit IgG HRP-conjugated antibody (Dianova, 111-035-144). Chemiluminescent signal was recorded with VILBER LOURMAT Fusion SL (Peqlab) and quantification was performed with ImageJ.

Mitochondria isolation

Cells were grown in 15 cm dishes and scrapped in cold PBS and pelleted at 500 g for 5 min. Cell pellets were resuspended in isotonic buffer (220 mM mannitol, 70 mM sucrose, 1 mM EDTA, 20 mM HEPES (pH 7.5) and 1 × protease inhibitor cocktail (Sigma-Aldrich, 05056489001) with 0.1% bovine serum albumin (BSA) (Pan-Biotech, P06-1394100). Cells were mechanically homogenized using syringe with 26G cannula for 15 strokes. Cell homogenate was centrifuged at 1000g for 10 min, supernatant was collected in fresh tube and further centrifuged at 10,000g for 10 min at 4°C to obtain crude mitochondrial fractions. Crude mitochondrial pellets were resuspended in isotonic buffer and Lowry assay was performed to determine the concentration. Crude mitochondrial fractions were aliquoted, centrifuged at 10,000g for 5 min and pellets were resuspended in freezing buffer (300 M trehalose, 10 mM KCl, 1 mM EDTA, 10 mM HEPES and 0.1% BSA) and stored in −80°C until further processing.

Co-immunoprecipitation

Mitochondrial aliquots of 500 μg were pelleted by centrifugation and re-suspended in isotonic buffer (150 mM NaCl, 10 mM Tris/HCl (pH 7.5), 5 mM EDTA, 1x protease inhibitor cocktail) with 10 μL of 10% Digitonin (2 g/g of protein) and solubilized for 10 min on ice. Solubilized proteins were centrifuged at 21,000 g for 20 min and 10% of the supernatant was separated as input fraction. Remaining supernatant were incubated with anti-Flag M2 affinity beads (Sigma) or MYC-Trap agarose beads (ChromTech) overnight in 4°C under rotation. For pulldown of MIC60, 1ug of MIC60 antibody (Abcam, ab110329) was conjugated with protein A Sepharose beads (Invitrogen, 101041). Excess antibodies from beads were washed out with PBS containing 1x protease inhibitor cocktail. Beads were centrifuged at 3700g for 1 min at 4°C. Beads were further washed (4x) with isotonic buffer with 0.01% digitonin. Proteins were eluted with Laemmli buffer without beta-mercaptoethanol at 65°C for 10 min with subsequent addition of 1 μL beta-mercaptoethanol and subjected to SDS-PAGE with subsequent western blotting.

Blue native gel electrophoresis (BN-PAGE)

Mitochondrial aliquots of 150μg were centrifuged and pellets were resuspended in 15 μL of solubilization buffer (50 mM NaCl, 2 mM aminohexanoic acid, 50 mM imidazole/HCl pH 7, 1 mM EDTA, protease inhibitor cocktail) with 3 μL of 10% digitonin (2 g/g of protein) and incubated on ice for 10 min. Samples were centrifuged at 21,000g for 10 min at 4°C and supernatant was collected in fresh tube followed by addition of 50% glycerol and 1.5 μL of 1% Coomassie brilliant blue G-250. Samples were loaded in 3–13% gradient gel and subsequently transferred on methanol activated PVDF membrane. Membranes were blocked in 5% skimmed milk for 1 h and incubation was carried out overnight in 4°C under shaking conditions with primary antibodies: MIC10 (Abcam, 84969), MIC13 (custom made by Pineda (Berlin) against human MIC13 peptide CKAREYSKEGWEYVKARTK), MIC19 (Proteintech, 25625-1-AP), MIC25 (Proteintech, 20639-1-AP), MIC26 (Thermofisher Scientific, MIC27 (Sigma-Aldrich, HPA000612-100UL), MIC60 (Abcam, ab110329), SLP2 (Abcam, ab102051), MTX1 (Abcam, ab233205). Primary antibodies were washed 3x with TBST and incubated with Goat anti-mouse IgG HRP-conjugated antibody (Abcam, ab97023) or goat anti-rabbit IgG HRP-conjugated antibody (Dianova, 111-035-144) diluted to 1:10000 in 5% skimmed milk in TBST. Chemiluminescent signal was recorded with VILBER LOURMAT

Fusion SL (Peqlab) and quantification was performed with ImageJ. For densitometry analysis, the intensity of MIC60 in each lane was measured to determine its incorporation into MICOS complexes. Coomassie staining was used to normalize for loading.

Mitochondria morphology analysis

Flp-In T-REx HEK293 cells were transfected with 1μg of mitochondrially targeted GFP (Mito-GFP) with along with 3.5 μL of GeneJuice. 24 h post transfection, cells were treated with 10 μM cycloheximide and incubated for 2 h at 37°C in CO_2 incubator. Media was removed following PBS washing three times. Cells were fixed using 4% paraformaldehyde (Sigma-Aldrich, P6148) for 20 min in room temperature and washed with PBS 3 times. GFP signals were visualized in PerkinElmer spinning disc confocal microscope equipped with a 60× oil objective. The analysis was performed in a double-blind fashion to eliminate any potential bias. Cells were categorized into one of four morphological classifications based on the predominant mitochondrial structure observed within each cell: hypertubular, tubular, intermediate, or fragmented. Cells classified as hypertubular contained large, extensively interconnected tubular mitochondrial networks. Cells classified as intermediate displayed a mix of mitochondrial forms, with a comparable ratio of short tubes and fragmented mitochondria, while cells classified as tubular and fragmented contained either mostly long tubular and very short mitochondria fragments, respectively.

Stimulated emission depletion (STED) nanoscopy

Cells were fixed and permeabilized as described earlier (PLA assay). Permeabilized cells were blocked with 5% goat serum and primary antibody incubation was carried out with 1:100 rabbit anti-MIC60 antibody (custom-made, Pineda (Berlin)), which was generated using the peptide CTDHPEIGEGKPTPALSEEAS against human MIC60, overnight at 4°C and 1:100 Aberrior STAR 635P goat-*anti*-rabbit (2-0012-007-2) secondary antibody incubated at room temperature for 1 h. STED imaging was performed with the Leica SP8 laser scanning confocal microscope coupled with an STED module. Initially, imaging of 80-nm gold particles (BBI Solutions) was carried out in reflection mode for correct alignment of excitation and depletion laser. A 93x glycerol (N.A = 1.3) objective was used with the pinhole set to 0.6 Airy units and a white light laser excitation wavelength of 633 nm was used for sample excitation. STED depletion was carried out with a pulsed STED depletion laser beam of 775 nm wavelength. A hybrid detector (HyD) was used for signal detection in the range from 643 to 699 nm. 13x magnification was used to acquire images covering a field of view of 9.62× 9.62 μm. No image processing was performed except smoothing carried out with Fiji software.[49] The analysis was performed in a double-blind manner, where each mitochondrion was categorized based on the predominant MIC60 punctate pattern into three distinct categories: rail-like, non-rail-like, or diffuse.

Electron microscopy

Cells were cultured in petri dishes until about 80% confluency was reached and chemical fixation was carried out using 3% glutaraldehyde buffered with 0.1 M sodium cacodylate, pH 7.2, followed by cell scrapping and centrifugation. Cell pellets were washed with 0.1 M sodium cacodylate and embedded in 2% agarose. Cell staining was performed with 1% osmium tetroxide for 50 min with subsequent incubation in 1% uranyl acetate/1% phosphotungstic acid for 1 h. Samples were further dehydrated with graded acetone series and embedded in spur epoxy resin for polymerization at 65°C for 24 h. Ultrathin sections of samples were prepared with microtome and images were captured with transmission electron microscope using Hitachi, H7100 or JEM -2100 plus (JOEL) and analyzed with ImageJ software. The images were randomized and the data was analyzed in a double-blind manner by two scientists. Data analysis was carried out by GraphPad prism. Outlier test was performed with Grubb's test where indicated using GraphPad Prism. Mitochondrial membranes from EM images were manually traced using Procreate software. Subsequently generated images were vectorized by Adobe Illustrator.

QUANTIFICATION AND STATISTICAL ANALYSIS

Data analysis was carried out by GraphPad prism. Student's *t*-test or one sample *t*-test was used for statistical analysis. The details regarding experimental replicates, data representation, and statistical analysis can be found in the figure legends. Probability (P) values are represented as follows: **p*-value $\leq$0.05, ***p*-value $\leq$0.01, ****p*-value $\leq$0.001, *****p*-value $\leq$0.0001, ns = non-significant, P-value >0.05.